

Trafficability Assessment of Deformable Terrain through Hybrid Wheel-Leg Sinkage Detection

Francisco J. Comin

Surrey Space Centre

University of Surrey, Guildford (UK)

f.comin@surrey.ac.uk

William A. Lewinger

Surrey Space Centre

University of Surrey, Guildford (UK)

w.lewinger@surrey.ac.uk

Chakravarthini M. Saaaj

Surrey Space Centre

University of Surrey, Guildford (UK)

c.saaaj@surrey.ac.uk

Marcus M. Matthews

Civil and Env. Engineering

University of Surrey, Guildford (UK)

m.matthews@surrey.ac.uk

Abstract

Off-road ground mobile robots are widely used in diverse applications, both in terrestrial and planetary environments. They provide an efficient alternative, with lower risk and cost, to explore or transport materials through hazardous or challenging terrain. However, non-geometric hazards that cannot be detected remotely pose a serious threat to the mobility of such robots. A prominent example of the negative effects these hazards can have is found on planetary rover exploration missions. They can cause a serious degradation of mission performance at best, and complete immobilisation and mission failure at worst. To tackle this issue, the work presented in this paper investigates the novel application of an existing enhanced-mobility locomotion concept, a hybrid wheel-leg equipped by a lightweight micro-rover, for in-situ characterization of deformable terrain and on-line detection of non-geometric hazards. This is achieved by combining an improved vision-based approach and a new ranging-based approach to wheel-leg sinkage detection. In addition, the paper proposes an empirical model, and a parametric generalization, to predict terrain trafficability based

on wheel-leg sinkage and a well-established semi-empirical terramechanics model. The robustness and accuracy of the sinkage detection methods implemented are tested in a variety of conditions, both in the laboratory and in the field, using a single wheel-leg test bed. The sinkage-trafficability model is developed based on experimental data using this test bed and then validated on-board a fully mobile robot through experimentation on a range of dry frictional soils that covers a wide spectrum of macroscopic physical characteristics.

1 Introduction

Reconnaissance and transport tasks on challenging, off-road terrains can be performed with lower risks and higher efficiency by using autonomous mobile robots. These benefits, which are valuable in terrestrial applications, are further amplified in planetary exploration missions. Wheeled locomotion provides a better trade-off between power efficiency, mobility and robustness than alternatives like tracked or legged rovers. However, non-geometric hazards that cannot be reliably detected remotely, e.g. sand traps or subsurface voids hidden by thin duricrusts or surface dust, threaten to temporarily or permanently immobilise these robots. Two possible approaches can mitigate this circumstance: improving the mobility of wheeled robots or detecting these non-geometric hazards in-situ.

Direct soil sensing devices, e.g. cone penetrometers (Zacny et al., 2010) or Bevameters (J. Wong, 1980), can reliably characterize the physical properties of the terrain, at the cost of high mechanical complexity, high power consumption and the need to stop the rover to take a measurement. These downsides can be avoided using indirect soil sensing techniques that aid detecting non-geometric hazards by analysing vehicle-terrain interaction on-the-fly while driving (Iagnemma, Kang, Shibly, & Dubowsky, 2004), e.g. through vibration-based classification (C. Brooks & Iagnemma, 2005; Weiss, Fechner, Stark, & Zell, 2007), slip detection (Ojeda, Cruz, Reina, & Borenstein, 2006; C. A. Brooks, Iagnemma, & Dubowsky, 2006; Iagnemma & Ward, 2009) or sinkage estimation (Reina, Ishigami, Nagatani, & Yoshida, 2008). On the other hand, the mobility of wheeled robots can be enhanced via passive or partially actuated suspensions, sometimes referred to as leg-wheeled, wheel-walking, rolling-walking or articulated-wheeled robots (Fu & Krovci, 2008). This improvement in mobility has been successfully demonstrated by the recent NASA rovers sent to Mars (Maimone, Cheng, & Matthies, 2007; Grotzinger et al., 2012).

While these developments can be effective when combined, they still require using overly cautious traversal speeds to detect the hazards and stop the rover before it is too late. This is especially aggravating in planetary

rover missions to Mars, due to the scarce and delayed communication links with Earth. Not only do the slow speeds significantly hinder mission performance and scientific return, but they also do not guarantee avoiding these hazards. All three Martian rovers that have exceeded 100 metres of driving have faced related issues, involving time-costly manoeuvres and detours in the best-case scenarios of Opportunity and Curiosity (David, 2005; Wall, 2014) and permanent immobilisation and mission termination for the worst-case scenario experienced by Spirit (Matson, 2010), as illustrated in Fig. 1 (left).

This paper presents a new approach to tackle this issue by further developing and combining enhanced wheeled mobility and indirect, on-line soil sensing through robot-terrain interaction analysis. It is proposed to use a hybrid locomotor concept that combines the control and mechanical simplicity of wheels with the higher mobility of legs. It consists of a single Degree of Freedom (DoF) rimless wheel, with its spokes acting as rotary legs, and its strengths and advantages have been thoroughly demonstrated in a variety of implementations (Saranli, Buehler, & Koditschek, 2001; Schroer, Boggess, Bachmann, Quinn, & Ritzmann, 2004). For the sake of conciseness and taking inspiration from Whegs (Quinn, Offi, Kingsley, & Ritzmann, 2002), the first robot family to use this concept with multiple spokes, this type of locomotor will be referred to in the rest of this paper as a wheel-leg. Although much research has been done previously on high-fidelity models (Ding et al., 2015), off-line stochastic characterisation (Gallina, Krenn, Scharringhausen, Uhl, & Schäfer, 2014), visual analysis (Skonieczny et al., 2014) or learned mobility prediction (Krebs, Pradalier, & Siegwart, 2010; Peynot, Lui, McAllister, Fitch, & Sukkarieh, 2014) for rimmed wheels interacting with deformable terrain, there is a lack of similar studies for the aforementioned multi-legged wheel-legs. Furthermore, the comparability of wheel and wheel-leg terrain interaction remains unaddressed.

The contributions of this paper include the combination and upgrade of existing wheel (Milella, Reina, & Siegwart, 2006) and wheel-leg (Al-Milli, Spiteri, Comin, & Gao, 2013) vision-based sinkage detection methods and the development of a novel ranging-based sinkage detection method using ground clearance estimation, for improved wheel-leg-soil interaction sensing. Both methods' accuracies and robustness are evaluated and compared in laboratory and field conditions. Moreover, an empirical model is developed and generalized using the same experimental set-up, in order to relate the sensed wheel-leg sinkage with terrain trafficability for wheels based on the tractive efficiency obtained from terramechanics models (Bekker, 1960). The new model is then independently validated on a fully mobile robot with two front wheel-legs on a range of dry frictional soil types with diverse physical strength characteristics.

These contributions enable the on-line and in-situ detection of non-geometric hazards, while the enhanced mobility of the wheel-leg reduces to a minimum the chances of the robot becoming permanently trapped.



Figure 1: Image of MER Spirit stuck on soft soil (left), courtesy of NASA (NASA, 2010), and conceptual illustration of the FASTER mission scenario (right), courtesy of the FASTER consortium (FASTER, 2013)

Such advances would be beneficial for both terrestrial and planetary applications. They can be applied on lone wheel-legged rovers, homogeneous wheel-legged multi-rover teams or heterogeneous teams, e.g. a wheel-legged Scout Rover (SR) assessing the terrain ahead of a heavier wheeled Primary Rover (PR), as proposed by the FP7 FASTER mission concept (Allouis et al., 2015; Nevatia et al., 2013; Lewinger et al., 2013) illustrated in Fig. 1 (right). The FASTER SR mobile robot itself, Coyote II (Sonsalla, Fritsche, Vögele, & Kirchner, 2013; Sonsalla, Ahmed, et al., 2014; Sonsalla, Nevatia, et al., 2014), was designed, built and provided by the German Research Centre for Artificial Intelligence (DFKI). It is not a contribution of this paper, and was only used as a platform for sensor system testing and algorithm validation.

The structure of the rest of the paper is the following: Section 2 introduces the operating principle, hardware and software design of the wheel-leg sinkage sensing system and the terramechanics model used for trafficability assessment; Section 3 describes the experimental set-ups, materials and testing methodology used; Section 4 discusses and compares the performance of the sinkage detection methods during testing; Section 5 goes through the development and validation of the empirical and generalized trafficability models based on wheel-leg sinkage; and Section 6 summarizes the conclusions of the work presented and indicates future work guidelines.

2 Wheel-Leg Sinkage Detection and Wheel Trafficability

Simulation

Multiple approaches have been explored to measure the level of sinkage in soil of a conventional rimmed wheel, using computer vision to analyse images of the wheel and to detect the wheel occlusion caused by that

sinkage (C. A. Brooks et al., 2006; Milella et al., 2006). Only one similar approach has been proposed for the hybrid wheel-leg concept (Al-Milli et al., 2013). However, this method is based on colour segmentation, which can be seriously affected by changes in environment lighting when High-Dynamic-Range imaging or an ad-hoc focused source of lighting are not available. In addition, it does not account for important operational factors, i.e. the tilting of the robot’s reference frame associated with the irregular rolling motion of wheel-legs and the presence of slopes or irregular dunes in the terrain. These issues are addressed in this paper through the improvement of the vision-based approach and the implementation of a new sinkage estimation method based on ground-clearance measurement.

2.1 Foot Designs and Wheel-Leg Configuration

The central component of the system is the wheel-leg itself, shown in Fig. 2 (a). It is closely based on previously used wheel-legs and further details of its design and fabrication processes can be found in (Hidalgo, 2013; Schwendner et al., 2009). It counts with five uniformly distributed spokes, with 180 mm length and 16 mm width. Each spoke consists of two full-length solid edges, bridged with the neighbouring legs for rigidity, and hollow space in the middle. While slightly compliant, the high stiffness provided by the design makes leg deflection negligible under the loads estimated for the FASTER SR used in this research (3.75 kg per wheel-leg). Interchangeable feet can be attached at the end of each leg. Three different designs are considered in this work, pictured in Fig. 2 (b). The rubber feet, similar to those used by the Asguard robots (Hidalgo, 2013), provide good load distribution, terrain adaptability and traction. The carbon fiber feet,

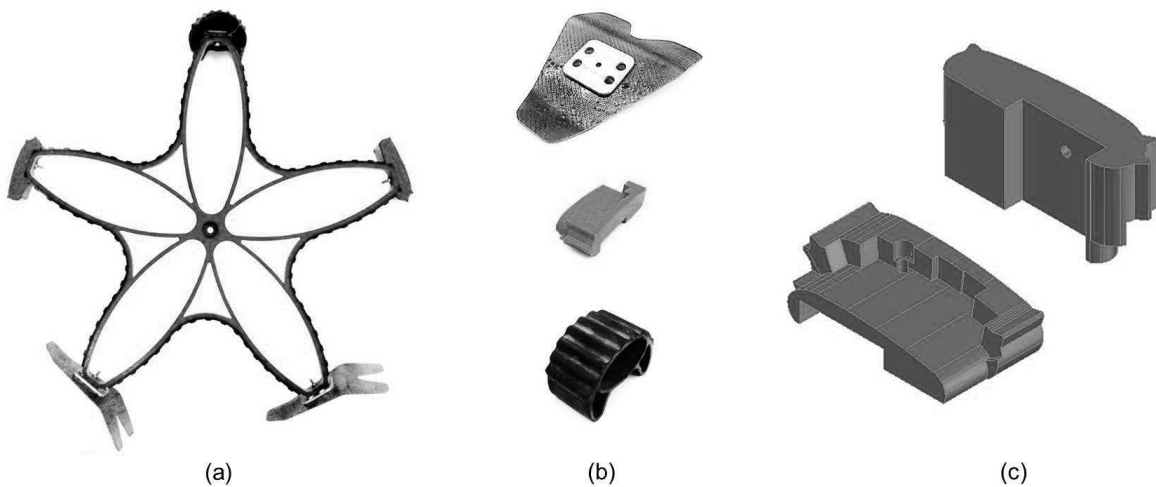


Figure 2: Wheel-leg and feet: (a) wheel-leg courtesy of DFKI (Sonsalla, Nevatia, et al., 2014) equipped with one rubber foot, two carbon fiber foot and two LTF wheel-leg, (b) individual pictures of a rubber foot (bottom), an LTF (centre) and a carbon fiber foot (top) and (c) two isometric CAD views of the LTF design

similar to those used by CESAR (Schwendner et al., 2009), have a much bigger contact area, considerably lowering the contact pressure in deformable terrain.

Finally, the Load Testing Feet (LTF) were specifically designed for the FP7 FASTER project. Their main design driver is to replicate the static contact pressure below one of the 10 cm-wide and 15 cm-radius wheels of the 350 kg FASTER PR with the reduced 15 kg mass of the SR. Figure 3 (left) plots as a blue line the average contact pressure below a PR wheel in Earth’s gravity, geometrically calculated for different sinkage levels of 0 – 120 mm. The initial width of the LTF is calculated to mimic the contact pressure with a 50% safety margin, shown as a dashed blue line, to ensure that the LTF would penetrate through any duricrust that is weak enough to break below the pressure of a PR wheel.

Due to the low mass of the SR, the resulting blade width is overly narrow. As a cautionary measure, to prevent excessive sinkage, the depth of this narrow blade is limited to 7 mm. This is enough to penetrate any sub-centimetre weak surface duricrusts as those reported by earlier Mars missions (Mutch, Arvidson, Binder, Guinness, & Morris, 1977; Arvidson et al., 2004), and acts as a maximum sinkage threshold for certainly safe terrain (‘GO’). Thereafter, the LTF is provided with a wider plateau, whose thickness is calculated to mimic the static pressure of a PR wheel at a sinkage of 75 mm. This is the specified maximum allowable sinkage for the FASTER PR, equal to half the wheel’s radius, and acts as the minimum sinkage for certainly unsafe

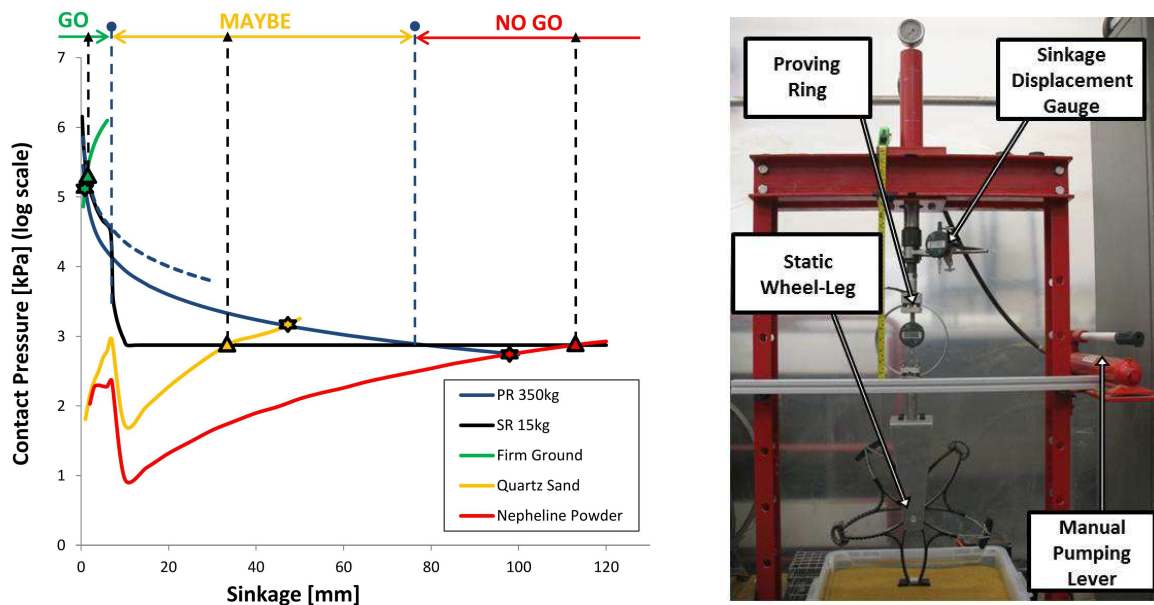


Figure 3: Pressure-sinkage curves geometrically calculated for PR wheel and a SR LTF and experimentally obtained for firm ground, quartz sand and nepheline powder (left) and static wheel-leg pressure-sinkage test set-up (right)

terrain (‘NO-GO’). Any sinkage level in between those thresholds is treated as uncertain (‘MAYBE’), as the contact pressure beneath a SR wheel-leg is significantly smaller than below a PR wheel in that region.

As a result of the final design, shown in two CAD isometric views in Fig. 2 (c), the geometrically calculated contact pressure below an LTF loaded with the SR nominal mass is shown as a black line in Fig. 3 (left). The red, yellow and green lines in the same plot correspond to experimental measurements of quasi-static pressure-sinkage tests on different types of materials using the LTF and the set-up shown in Fig. 3 (right). The manually actuated hydraulic press slowly increases the force applied on the wheel-leg through a proving rim that measures this force. Two digital displacement gauges are recorded simultaneously to measure the sinkage and proving ring deflection.

The initial peaks in the experimental curves correspond to the high pressure due to the small contact area of the LTF blade. This is followed by a drop due to the higher contact area of the LTF plateau and a constant increase thereafter, as expected from the pressure-sinkage behaviour of soils. The intersections between these lines and the geometrically calculated ones (triangle and star markers) correspond to the expected static sinkage of a SR wheel-leg and a PR wheel respectively. The intersection sinkages for each medium exemplify how the LTF static sinkage thresholds would classify the negligible-sinkage rigid surface as a ‘GO’, the mid-sinkage quartz sand as a ‘MAYBE’ and the high-sinkage fine nepheline powder as a ‘NO-GO’.

It should be remarked that the sinkage of an LTF can only mimic that of a PR wheel accurately on static loading conditions, with a leg normal to the terrain. During dynamic rolling motion, the varying attack angle of the leg generates a pushing-rolling regime that affects the penetration stresses (C. Li, Zhang, & Goldman, 2013). This consideration, which would still be true if the wheel-leg had the same radius as the PR wheel, increases the certainty of the LTF breaking through thin duricrusts. However, it raises the question of whether this is a reliable criterion to evaluate terrain trafficability, which will be addressed in Section 5.

2.2 Proprioceptive sensing of wheel-leg attitude and stance-cycle phase

The main difference between visually detecting sinkage on conventional rigid wheels and wheel-legs is that the latter have an irregular, dynamic shape in the Field of View (FoV) of the camera and it causes rapid changes in the attitude of the rover’s body. Therefore, the absolute angular position of each leg of the sensed wheel-leg ($\theta_{L,i}$) needs to be reported to put the measurements from the other sensors in context. This angle is measured clockwise around the positive Y-axis of the robot body reference frame (Y_R) with its zero value

on the negative Z-axis of said frame (Z_R). Additionally, an estimate of the attitude of the robot's body is required, which can be obtained from a 6-DoF Inertial Measurement Unit (IMU). The algorithm used for attitude estimation is based on the explicit complementary filter presented in (Mahony, Cha, & Hamel, 2006), yielding the roll (ϕ_R) and pitch (ψ_R) angles of the robot body reference frame.

To analyse the wheel-leg-soil interaction, a key variable is the minimum angle formed by any of the legs and the direction of the gravity vector (θ_W), defined in Eq. (1). The continuous motion of the wheel-leg can be then sub-divided into quantized, periodic leg stance cycles with $\theta_W \in [-\alpha/2, \alpha/2]$, where α is the angle between two consecutive legs, i.e. $2\pi/n_L$ radians for a wheel-leg with n_L legs.

$$\theta_W = \min_{i \in [1, n_L]} (\theta_{L,i} - \psi_R) \quad (1)$$

For a multi-spoked wheel-leg rolling on deformable terrain, unlike previous models considering perfectly rigid terrain (Coleman, 2010) or single-legged wheel-legs (C. Li et al., 2013), more than one leg can be simultaneously in contact with the ground. One leg stance cycle is then divided into three distinct phases: an initial Double Leg Stance (DLS) that ends with the lifting from the ground of the trailing foot, an intermediate Single Leg Stance (SLS) during which only the middle leg is on the ground and a final Double Leg Stance that starts with the impact of the leading foot onto the ground. The Single Leg Stance phase can be also sub-divided into the contact phase (pre-midstance) and propulsive phase (post-midstance). The Triple Leg Stance (TLS) phase, during which three legs are simultaneously in contact with the ground is considered out of scope for this study. These phases, sketched in Fig. 4 (left), can be represented through a stance phase plot, in the space defined by θ_W and the maximum sinkage experienced by any leg in contact with the terrain (ζ_z), as in Fig. 4 (right).

The boundaries between the Single Leg Stance and Double Leg Stance correspond to the loci of possible foot lifting and impact events for a given leg length (l_L) and longitudinal terrain inclination (ψ_T), where the

impact (θ_W^I) and lifting (θ_W^L) wheel-leg angles follow the expressions in Eq. (2).

$$\left. \begin{aligned} \theta_W^L &= -\alpha/2 + \arcsin\left(\frac{\zeta_z \cos \psi_T}{2l_L \sin \alpha/2}\right) - \psi_T \\ \theta_W^I &= \alpha/2 - \arcsin\left(\frac{\zeta_z \cos \psi_T}{2l_L \sin \alpha/2}\right) - \psi_T \end{aligned} \right\} \rightarrow \left\{ \begin{array}{ll} \text{Foot Lifting} & \text{if } \theta_W = \theta_W^L \\ \text{SLS Contact Phase} & \text{if } \theta_W \in (\theta_W^L, 0) \\ \text{SLS Midstance} & \text{if } \theta_W = 0 \\ \text{SLS Propulsive Phase} & \text{if } \theta_W \in (0, \theta_W^I) \\ \text{Foot Impact} & \text{if } \theta_W = \theta_W^I \\ \text{DLS} & \text{otherwise} \end{array} \right. \quad (2)$$

Dynamic assessment of the sinkage throughout each of these phases is feasible and potentially useful. However, maximum contact forces are generated during the contact phase of the Single Leg Stance (C. Li et al., 2013), indicating that dynamic sinkage events are likely to occur between foot impact and midstance. In consequence, the sinkage level detected at midstance is taken as the indicator for each stance cycle, in the interest of computational and analysis simplicity.

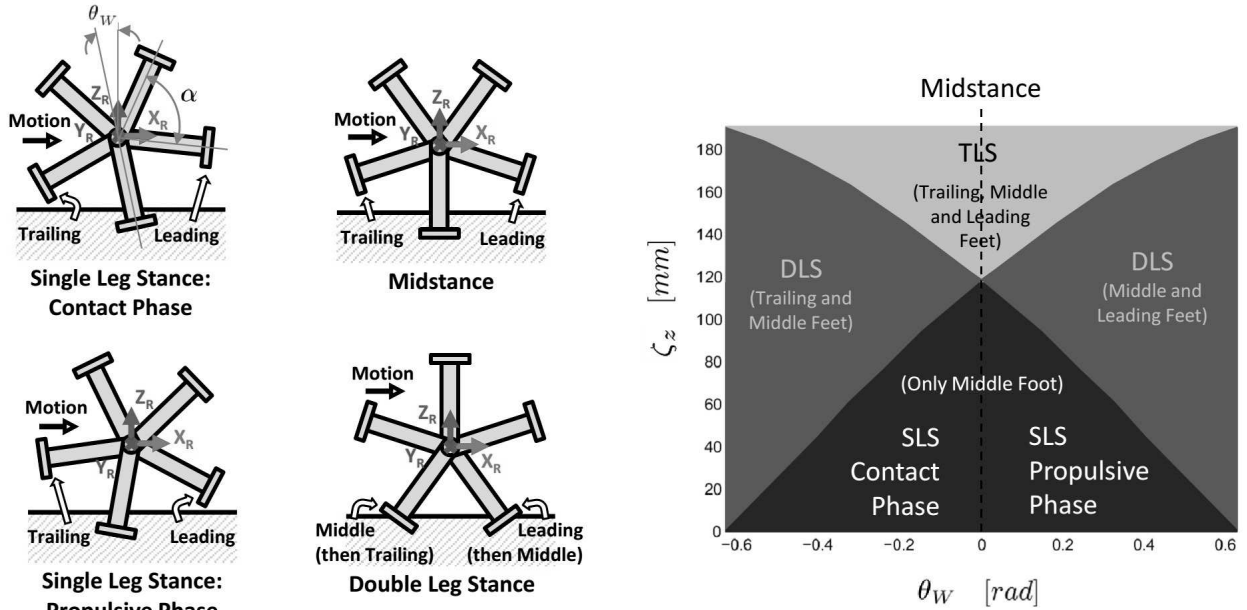


Figure 4: Main stages and events of a typical wheel-leg stance cycle (left) and stance phase plot for the wheel-leg on flat terrain, i.e. $\psi_T = 0$ (right)

2.3 Exterioceptive sensing of wheel-leg sinkage

The level of sinkage of the wheel-leg is inferred from exteroceptive sensor data regarding the location of the terrain relative to the SR body frame. Two complementary exteroceptive sensing modalities are explored: an Infrared Ranger (IR) mounted on the underside of the SR chassis pointing downward to measure the ground clearance, and a camera focused on the wheel-leg to detect the level of occlusion of its legs as they sink into the ground. Combining these data with the sensed absolute position and attitude of the wheel-leg and the fact that the reference frames of the IR and the camera are rigidly attached to the robot’s body reference frame permits the estimation of wheel-leg sinkage.

Ranging-based ground clearance estimation

Infrared range finders are extensively used in diverse mobile robotic applications. Most of them involve obstacle avoidance (Benet, Blanes, Simó, & Pérez, 2002) and target tracking (T. Li, Chang, & Tong, 2004). The applications to terrain characterization (Ojeda, Borenstein, Witus, & Karlsen, 2006) are rarer, and are mostly limited to conventional wheeled mobile robots focusing on indirect terrain classification rather than on explicit sinkage detection. Infrared range finders are selected over ultrasonic range finders due to the poor performance of the latter on porous materials, e.g. granular soils. One of the main downsides of infrared rangefinders is their sensitivity to changes in environmental lighting and to reflectance properties of the sensed media. However, the IR is mounted on the underside of the rover chassis, thus being protected by its shade from most variations in ambient lighting and direct exposition to the sun. Any outstanding, low frequency light disturbances can be filtered further by using high-frequency modulated infrared signals. Moreover, the IR sensors used show negligible sensitivity to variations in material reflectance in the 18-100% range for $0.8 - 1.0 \mu\text{m}$ wavelength radiation, which covers the vast majority of naturally occurring terrestrial and planetary terrains (Manduchi, Castano, Talukder, & Matthies, 2005; Pommerol, Schmitt, Beck, & Brissaud, 2009).

Assuming that the terrain is flat ($\phi_T = \psi_T = 0$) and the IR is placed below the rotational symmetry axis of the wheel-leg ($x_w = 0$), the IR-based sinkage estimate ($\zeta_{z,IR}$) can be expressed as a function of the length of a leg, the roll and pitch angles of the robot relative to the world reference frame, the absolute angular position of the wheel-leg, the position of the IR relative to the rotation centre of the wheel-leg ($[x_w, y_w, z_w]$) and the clearance measured by the IR (z_{IR}) as shown in Eq. (3) and illustrated in Fig. 5 (top).

$$\zeta_{z,IR} = (l_L \cos(\theta_L - \psi_R) + y_w \tan \phi_R - (z_{IR} + z_w) \cos \psi_R) \cos \phi_R \quad (3)$$

It is worth considering that, if the assumption of flat terrain is violated, the formula in Eq. (3) will be subject to errors. The magnitude of these errors will depend on the transversal (ϕ_T) and longitudinal (ψ_T) inclination angles of the terrain, as expressed in Eq. (4) and depicted in Fig. 5 (bottom). For the experimental set-up used in this work ($z_w = 60$ mm, $y_w = 100$ mm, $l_L = 180$ mm and $\zeta_z \in [0, 75]$ mm), the relative estimation errors at ± 5 deg transversal and longitudinal slopes are $e_\phi \approx 3\%$ and $e_\psi \approx 5\%$ respectively. The errors are minimized when the IR is placed as close as possible to the wheel-leg ($y_w \rightarrow 0$) and when the leg is aligned with the IR beam ($\theta_L \rightarrow 0$). Whether these errors produce an underestimation or overestimation of the sinkage level depends on the orientation of the incline, the attitude of the rover's reference frame and the angular position of the wheel-leg.

$$e = e_\phi \cos \psi_R + e_\psi \cos \phi_R \begin{cases} e_\phi = \left((z_{IR} + z_w) \sin \phi_R + y_w \cos \phi_R - \left(l_L - \frac{\zeta_z}{\cos \psi_R \cos \phi_R} \right) \sin \phi_R \right) \tan \phi_T \\ e_\psi = \left((z_{IR} + z_w) \sin \psi_R - \left(l_L - \frac{\zeta_z}{\cos \phi_R \cos \theta_W} \right) \sin \theta_W \right) \tan \psi_T \end{cases} \quad (4)$$

Significant errors due to uneven terrain can be potentially alleviated if a sufficiently accurate elevation map of the terrain is available, by using terrain inclinations as an input to the estimation algorithm. Excessively rough surfaces, e.g. boulder fields or high-frequency acute dunes, might render this method overly inaccurate. However, such circumstances fall into the category of geometric hazards, and can be detected in advance

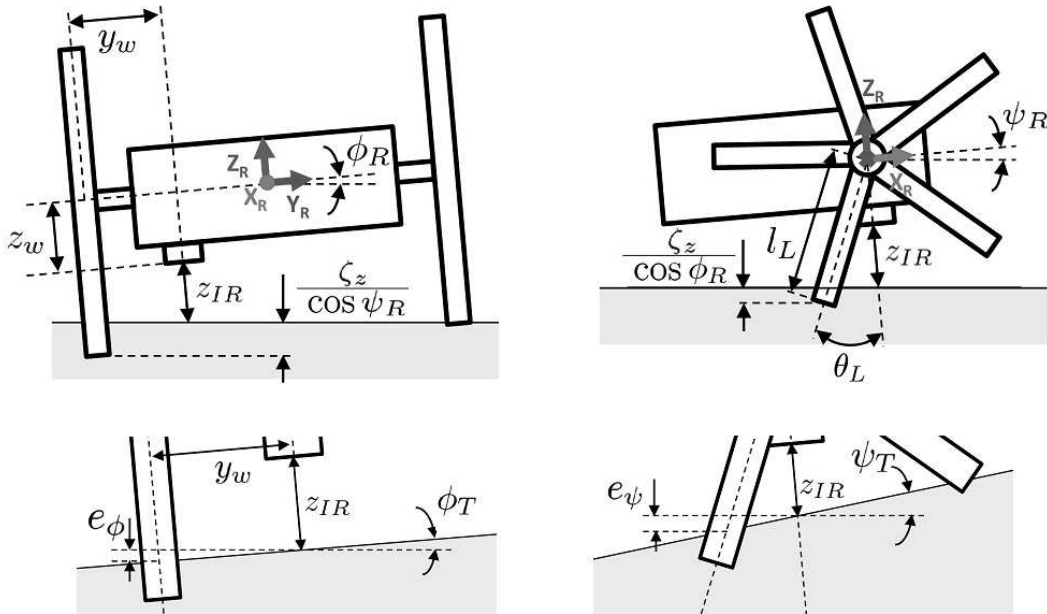


Figure 5: Dimensions and variables involved in sinkage estimation based on ground clearance (top) and errors induced by terrain inclination (bottom) in the transversal (left) and longitudinal (right) directions

through remote sensing (Helmick, Angelova, & Matthies, 2009; Howard & Seraji, 2001) in order to ignore potentially spurious in-situ sinkage estimates or directly avoid traversing them.

Vision-based leg occlusion detection

The approach used for vision-based sinkage detection aims at segmenting the irregular, rotating legs of the wheel-leg from the image background, similarly to the method presented in (Al-Milli et al., 2013). But rather than using a colour-based algorithm, which can be extremely sensitive to lighting and background conditions, an edge detection algorithm is applied. Inspiration is taken from the method published in (Milella et al., 2006) for conventional wheels, adapting it to wheel-legs by substituting the radial black and white pattern with 1 mm thick black and white stripes attached to both edges of each leg, perpendicular to the radial centreline of the corresponding leg as shown in Fig. 6 (d). The edge detection algorithm proposed by Canny (Canny, 1986) is used to detect the pattern attached to the leg. This method is chosen over other edge detection algorithms, e.g. Prewitt’s operator or Zero-Crossing, due to its higher robustness to noise in spite of its higher computational cost.

Firstly, a Gaussian filter is applied to smooth the image and reduce the noise. Choosing a small size of the Gaussian kernel favours the detection of fine features like the black and white pattern. Next, the Sobel operators in the X and Y directions are applied to obtain the intensity gradient’s magnitude and quantized direction, which enables a process of non-maxima suppression that yields a single pixel line along detected edges. Two hysteresis thresholds are applied, rejecting any edges with a gradient value below the lower threshold and accepting all edges with a gradient value above the higher threshold. Edges in-between both thresholds are only accepted when they neighbour a valid edge. The upper:lower threshold ratio recommended by Canny is between 2:1 and 3:1. However, slightly increasing the lower threshold aids in filtering background edges that do not belong to the leg pattern as exemplified in Fig. 6 (a).

The next step is to smooth down the edges through successive morphological operations on the processed image, so as to merge contiguous edges leading to the formation of a single contour of the leg’s black and white pattern as depicted in Fig. 6 (b). The choice of kernel size and number of iterations of these morphological operations is critical to successfully filter unrelated edges detected in the previous step and merging only the edges of interest. However, once the appropriate parameters have been selected for the given configuration, the algorithm is robust to changes in background and lighting condition. The empirically determined parameters used in this particular implementation are shown in Table 1.

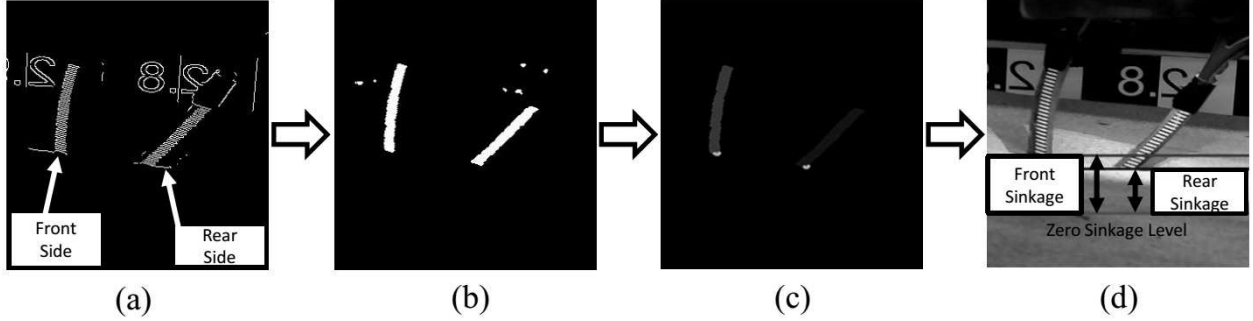


Figure 6: Steps of vision-based leg occlusion detection: (a) edge detection, (b) edge merging, (c) interface detection and (d) sinkage calculation

Table 1: Parameters of edge detection and merging algorithm

Image Capture		Canny Edge Detection			Morphological Edge Merging		
Resolution	r_{px2mm}	Upper Th.	Lower Th.	Kernel Size	Kernel Shape	Kernel Size	Iterations
800x600	0.5	450	300	3x3	Ellipse	3x3	6

Another crucial improvement relative to the approach presented in (Al-Milli et al., 2013) is that each side of the leg is considered separately and no masking is applied on the image. Any remaining background noise after the edge merging phase is filtered out by detecting the closed contours in the image and selecting only those two with largest area, corresponding to both sides of the leg, as marked in grey in Fig. 6 (c). Finally, the lower pixels of the boundaries of the selected contours are considered as the leg-soil interfaces. Their average Y-coordinates in the image frame are calculated ($y_{px,L}$ and $y_{px,R}$ for left and right sides of the leg respectively), shown in white in Fig. 6 (c) and as horizontal lines in Fig. 6 (d). The previously calibrated Y-coordinate values of zero occlusion for the corresponding wheel-leg angular position ($y_{px,0}(\theta_L)$), marked by the lowest horizontal line in the same image, are used to estimate the sinkage ($\zeta_{z,VBS}$) together with the known pixel-to-mm ratio of the wheel-leg plane in the image frame (r_{px2mm}) and the pitch of the robot reference frame, as in Eq. (5).

$$\zeta_{z,VBS} = \frac{y_{px,0}(\theta_L) - (y_{px,L} + y_{px,R})/2}{\cos \psi_R} r_{px2mm} \quad (5)$$

Faulty leg detection cases, e.g. due to a single contour detected for a leg with low sinkage levels or due to background contours bigger than the leg sides for high sinkage levels, are corrected during the contour selection stage by selecting a single contour when a minimum area requirement is not fulfilled by the second largest contour. Both the Vision-Based Single-Sided (VBSS), using only the biggest closed contour, and the Double-Sided (VBDS) leg sinkage detection approaches are implemented with the edge detection and

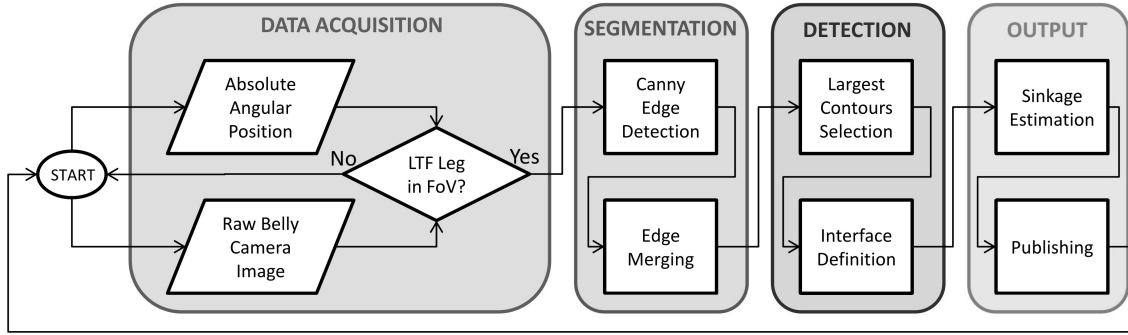


Figure 7: Flow chart of sinkage estimation algorithm based on edge detection and merging

merging method to compare their computational performance and accuracy. The algorithm flow for both cases is represented in Fig. 7, with differences only in the *Largest Contour(s) Selection* stage, where either one (VBSS) or two (VBDS) contours are selected for use in subsequent stages.

While the robustness of the algorithm might be enough by itself in normal lighting conditions, it can still fail when approaching the exposure limits of the camera sensor, i.e. very high or very low luminosity. An example of such a failure can be seen in Fig. 8 (a), where the colour-based algorithm from (Al-Milli et al., 2013) fails to detect the blue colour of the leg due to the strong background light source. Such flaws could be avoided using camera sensors with High-Dynamic-Range imaging capabilities, but this is not the case of the chosen camera for this implementation. Instead, a workaround was used where ad-hoc high-intensity white LEDs were installed focusing on the leg to create a dominant source of lighting on the object of interest. This addition not only corrects the problems with high background luminosity as shown in Fig. 8 (b) but also allows vision-based sinkage detection algorithms to operate in dark environments as in Fig. 8 (c). The set-up was tested in a variety of indoor and outdoor environments, as shown in Fig. 8 (d) and Fig. 8 (e), proving correct operation in the vast majority of cases, even with intense sun back light.

2.4 Hardware and Software Implementation

Both the hardware and the software implementation of the wheel-leg sinkage detection sensor system were designed to maximize modularity and re-reconfigurability, so as to enable the system to be tested as a standalone unit in simplified test beds and to facilitate its integration with different fully mobile robotic platforms. Commercial off-the-shelf and open source components were used, illustrated in Fig. 9 together with the data interfaces and the main functionalities of each level.

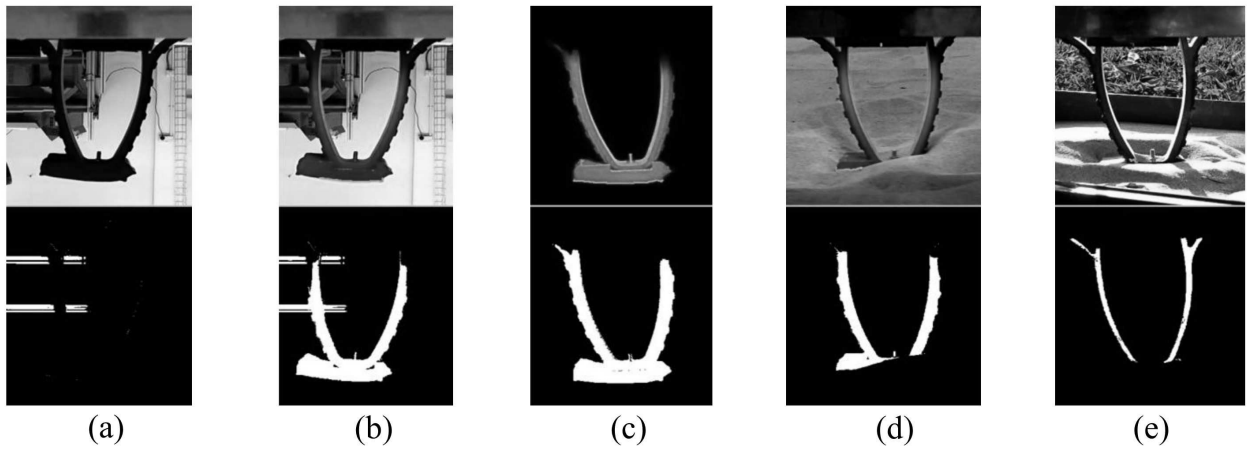


Figure 8: Raw image (top) and binary segmented image using the colour-based sinkage detection algorithm (bottom) with (a) intense background glare and no LEDs, (b) intense background glare and LEDs, (c) complete darkness and LEDs, (d) indoor lighting and (e) outdoors with sun back light

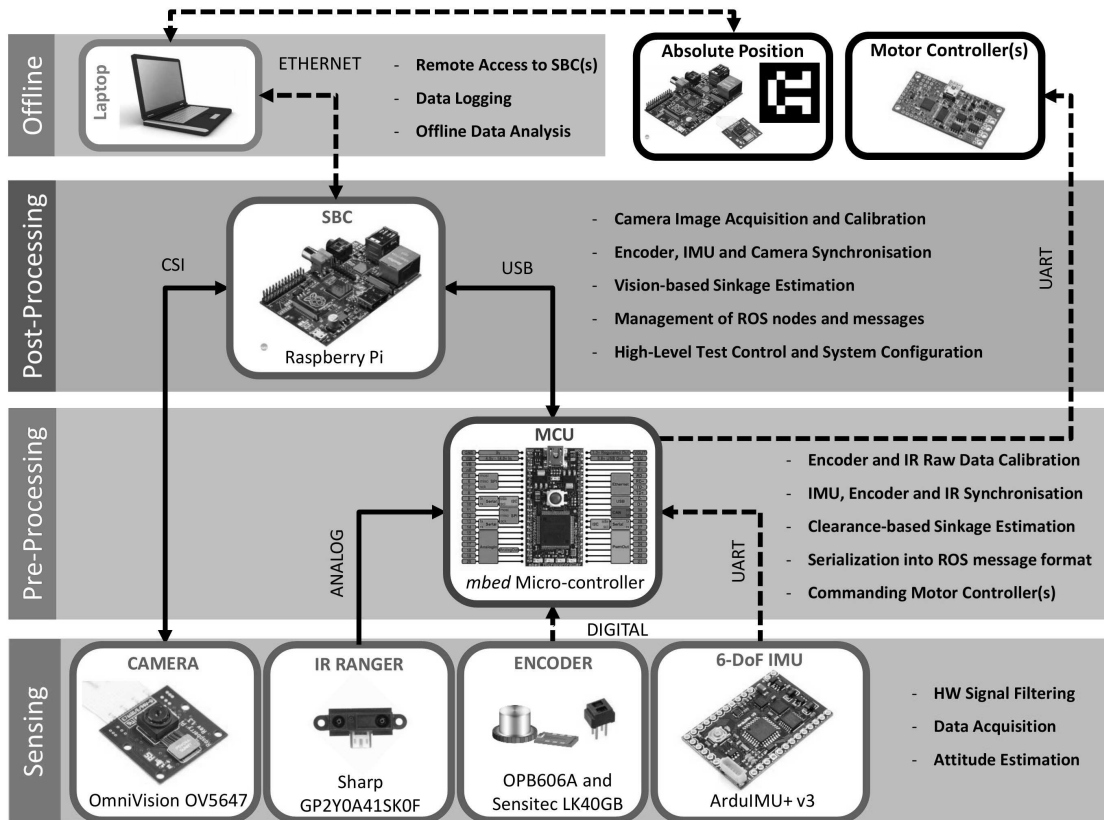


Figure 9: Main hardware components, data interfaces and functionalities

Four basic sensing units are combined. An analogue IR (Sharp GP2Y0A41SK0F), with 4 – 30 cm sensing range and 40 kHz signal modulation. A magnetoresistance-based absolute angular position encoder (LK40GB) mounted directly on the output shaft of the DC motor gearbox, with three digital channels and 0.1 deg resolution. An open-source 6-axis IMU (ArduImu+ v3), with an on-board 20 MHz Atmega328 microprocessor to distribute part of the computational load by sampling the gyroscopes and accelerometers, performing the attitude estimation and broadcasting the results through an UART connection. A CMOS QSXGA camera sensor (OV5647), with 54x41 deg FoV and 30 fps frame rate. The camera is directly connected for fast image acquisition through a Camera Serial Interface (CSI) to a Single-Board Computer (SBC) with a 700 MHz ARM11 CPU and a 250 MHz GPU. The rest of the sensors are interfaced with a 96 MHz Cortex-M3 Micro-Controller Unit (MCU) for data acquisition, calibration, synchronisation and clearance-based sinkage estimation according to Eq. (3).

The Robotic Operating System (ROS) framework is used to implement the software architecture, taking benefit of its ability to distribute the computational load between networked machines. The MCU works with a C/C++ compiler and is able to communicate directly with ROS nodes running on a Linux machine

via-USB thanks to the *rosserial* package. In this case, it is connected to the SBC, which runs a ROS Master, manages the nodes and message topics and controls the tests. The SBC is connected through Ethernet to another Linux machine, initially a laptop, for remote access and data logging. The nodes log timestamped raw and processed data in CSV files for off-line importation, post-processing and analysis using MATLAB. The laptop is also connected to an additional SBC-camera system for on-line absolute position sensing, using the ARUCO marker library (Garrido-Jurado, Muñoz-Salinas, Madrid-Cuevas, & Marín-Jiménez, 2014). The MCU can be also used to send commands to DC motor controllers used to drive the actuators during test execution. All dashed lines indicate non-fundamental connections, meaning that the system can be easily and even dynamically re-configured to remove these connections and gather the required information from alternative sources, e.g. from sensors readily available on-board the SR via-software from the SR On-Board Computer (OBC).

2.5 Terramechanics-based Wheel-Soil Interaction Model

In order to predict the trafficability of the terrain for a wheeled vehicle, e.g. the FASTER PR, the thoroughly researched semi-empirical terramechanics model for rigid wheels interacting with deformable terrain is applied. This model is based on the assumptions of a quasi-static, steady interaction, where the total reaction forces of the soil can be computed through the integration of the stresses generated on the wheel-soil interface. Alternative dynamic models have been proposed (Irani, Bauer, & Warkentin, 2011), but the mean values show good agreement with the quasi-static approach.

Normal stresses (σ) can be modelled as a non-linear function of sinkage (z) applying Bekker's equation (Bekker, 1960), based on the earlier Bernstein-Goriatchkin model. Shear stresses (τ) can be calculated using Mohr-Coulomb's failure criterion and Janosi's shear-displacement model (Janosi & Hamamoto, 1961), resulting in a function of the normal stress and the slip ratio (i). Finally, if the wheel is provided with grousers for better traction, as is the case for the FASTER PR, the shear stresses produced by them can be modelled as passive lateral earth pressure following Rankine's failure theory.

$$\begin{cases} \sigma(z) = (k_c/b + k_\phi) z^n = k_{eq} z^n \\ \tau(\sigma, i) = (c + \sigma(z) \tan \phi) \left(1 - e^{-\frac{\sigma}{K} [\theta_1 - \theta - (1-i)(\sin \theta_1 - \sin \theta)]} \right) \\ p_g(z) = \gamma z \tan^2 (\pi/4 + \phi/2) + 2c \tan (\pi/4 + \phi/2) \end{cases} \quad (6)$$

The resulting expressions for each of these stresses, summarized in Eq. (6), depend solely on soil parameters

and the level of slip and sinkage of the wheel. The sinkage of the wheel can be defined in polar coordinates as a function of the entry and exit contact angles (θ_1, θ_2) and the angle of maximum normal stress (θ_m) . The latter is dependent on wheel slippage, and a common assumption is to neglect rut recovery $(\theta_2 = 0)$, thus leading to the following expression for sinkage:

$$z(\theta, \theta_1, \theta_m) = \left\{ \begin{array}{ll} R(\cos \theta - \cos \theta_1) & , \quad \theta > \theta_m \\ R \left[\cos \left(\theta_1 - \theta \frac{(\theta_1 - \theta_m)}{\theta_m} \right) - \cos \theta_1 \right] & , \quad \theta < \theta_m \end{array} \right\} \quad \theta_m(\theta_1, i) = (c_1 + c_2 i) \theta_1 \quad (7)$$

The net vertical (F_V) and horizontal (F_H) reaction forces result from the integration of the interface stresses, as per Eq. (8) and Eq. (9) respectively for a wheel with radius R . Based on the assumption of a sufficiently wide wheel, uniform transversal stress distributions across the wheel's width (b) are considered, hence reducing the problem to two dimensions. The interaction stresses and forces are depicted together with the main dimensions involved in the model in Fig. 10 (left).

$$F_V = b \left[\int_{\theta_m}^{\theta_1} \sigma(\theta) \cos \theta R d\theta + \int_0^{\theta_m} \sigma(\theta) \cos \theta R d\theta \right. \\ \left. + \int_{\theta_m}^{\theta_1} \tau(\theta) \sin \theta R d\theta + \int_0^{\theta_m} \tau(\theta) \sin \theta R d\theta \right] \quad (8)$$

$$F_H = F_T - F_R = b \left[\frac{N_g \theta_1}{2\pi} \int_0^{h_g} p_g(z) dz + \int_{\theta_m}^{\theta_1} \tau(\theta) \cos \theta R d\theta + \int_0^{\theta_m} \tau(\theta) \cos \theta R d\theta \right] \\ - b \left[\int_{\theta_m}^{\theta_1} \sigma(\theta) \sin \theta R d\theta + \int_0^{\theta_m} \sigma(\theta) \sin \theta R d\theta \right] \quad (9)$$

These are complex integrals without a closed-form solution. Some approximations, e.g. the linearisation of normal stress distributions (Iagnemma et al., 2004), can simplify their calculation. However, these are not applied here. Instead, numerical integration using Simpson's rule is used. An iterative process is applied, gradually increasing the entry contact angle until the weight applied on the wheel $(W = Mg)$ is compensated and vertical force equilibrium is achieved, as illustrated in the flow diagram of Fig. 10 (right).

The steady-state contact stresses are then used to compute the net horizontal traction force, commonly referred to as draw-bar pull. A good metric to quantify the trafficability of the terrain is the tractive efficiency of the wheel (η_d) . This magnitude comprises the mobility efficiency (η_m) and slip efficiency (η_s) . The former

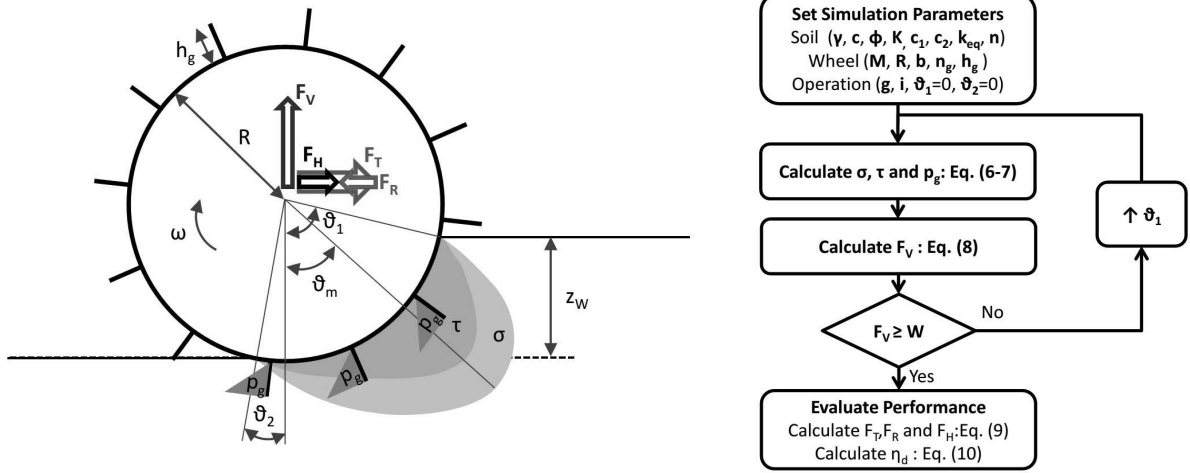


Figure 10: Dimensions, stresses and forces involved in the terramechanics model for driven rigid wheels on deformable terrain (left) and execution flow of the parametric numerical simulation (right)

evaluates the ratio between the net thrust force and the total thrust generated, i.e. the complement of the total negative resistive forces (F_R) over the positive thrust force (F_T). The latter reflects how much of the wheel's rotation results in effective traversing motion, i.e. the complement of the slip. The terrain-independent electrical-to-mechanical efficiency curve (Broderick, Tilbury, & Atkins, 2014) is not considered here, in order to focus on the terrain-dependent aspects of wheel tractive efficiency.

$$\eta_d = \eta_m \eta_s = \frac{F_H}{F_T} \frac{v}{\omega R} = \left(1 - \frac{F_T - F_H}{F_T}\right) \left(1 - \frac{\omega R - v}{\omega R}\right) = \left(1 - \frac{F_R}{F_T}\right) (1 - i) \quad (10)$$

The global efficiency, expressed in Eq. (10), yields a value between 0 and 1, penalized by both high slip and soil resistance forces. While negative values are technically possible, i.e. when the resistive forces overcome the thrust forces, this circumstance involves that the wheel is being towed rather than self-driven and hence the soil is non-trafficable for that wheel. Therefore, negative tractive efficiencies are saturated to zero.

3 Experimental Set-ups, Methodology and Results

Sensing and analysing the interaction of vehicles with different types of terrain, whether using analytical (J.-Y. Wong & Reece, 1967), empirical (Kim & Lee, 2013) or numerical (Perumpral, Lilledahl, & Perloff, 1971) methods, require experimental validation of the accuracy of the analysis and the functionality of the sensors. This can be done either using a simplified physical model with a single locomotor, for better control

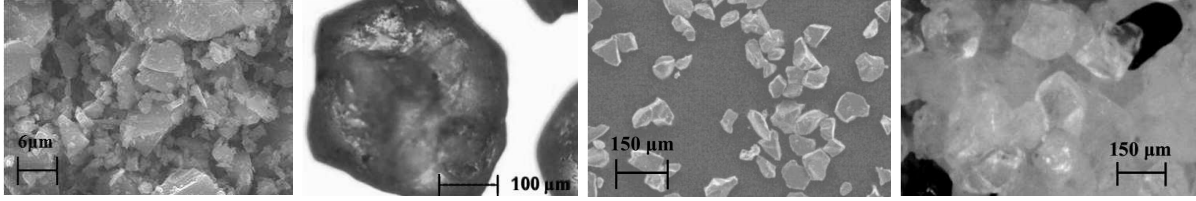


Figure 11: Microscope images of Martian soil simulants (from left to right) ES-1, ES-3, SSC-2 and SSC-3

Table 2: Principal physical characteristics of soil types used

Soil Type	Particle Shape	Particle Size [μm]	c [kPa]	ϕ [deg]	k_{eq} [kPa/m^{n-1}]	n
ES-1	Angular	0.92 ± 0.61	1.42	29.67	64.64	0.69
ES-3	Sub-rounded	456 ± 180	0.82	35.09	971.03	0.76
SSC-2	Angular	53 ± 16	1.72	42.42	370.53	0.58
SSC-3	Sub-angular	247 ± 62	0.79	30.13	995.74	1.01

and repeatability of testing conditions, or using a fully mobile platform, for more representative operation scenarios. This research combines both, using a Single Wheel-Leg Test Bed (SWLTB) for initial testing and the FASTER SR prototype for final validation.

3.1 Soil Types and Physical Characteristics

Different types of characterised soil are used during experimentation to evaluate the sensitivity of the sinkage detection approaches to changes in the characteristics of the terrain under the same operational conditions and to relate the detected wheel-leg sinkage to terramechanics-based trafficability.

During the laboratory testing campaign, four different types of soils were used (Gouache et al., 2011; Scott & Saaaj, 2012). Due to the special interest on the application to planetary exploration the soils used are dry, frictional sands with low cohesion. They include: a very fine nepheline powder (ES-1), a coarse quartz-based sand (ES-3), a fine garnet-based silt (SSC-2) and a medium sized quartz sand (SSC-3). Microscopic images of all four types of soil are shown in Fig. 11. As seen from these images, the four types of soil cover a variety of particle shapes and sizes, which reflect in different macroscopic physical properties. The shear-displacement (c, ϕ, K) and pressure-sinkage (k_{eq}, n) parameters were measured using Bevameter plate and direct shear tests.

The microscopic and macroscopic characteristics summarized in Table 2, including particle shape and mean particle size with one standard deviation, demonstrate the wide range of physical properties covered by these soils. ES-3 and SSC-3 have similarly high pressure-sinkage stiffness, but the latter has a significantly lower

internal friction angle. SSC-2 demonstrates the highest shear strength in spite of its lower pressure-sinkage stiffness. Finally, ES-1 has the lowest values for both pressure-sinkage and shear-displacement parameters, therefore being expected to have the lowest trafficability of all four soils.

3.2 Single Wheel-leg Test Bed

The SWLTB used for testing is pictured in Fig. 12. An extruded aluminium frame is mounted on a moving carriage, driven by a wheeled mechanism over two guiding rails that extend over a 5 m long and 18 cm deep box full of regolith. A rigid assembly contains the driven wheel-leg, and the sensors and electronics to detect wheel-leg sinkage and to control the speed of both motors driving the wheel-leg and the moving carriage. This wheel-leg assembly is attached to the moving carriage through a single passive rotary DoF, with its rotation axis horizontally orthogonal to the direction of driving to simulate the characteristic tilting motion caused by the irregular shape of the wheel-leg as it rolls.

The DC motor used to drive the carriage is rated at 250 W and 2750 rpm, with a 174.9:1 gearbox. The carriage-driving wheel is always loaded against the guiding rail, which is covered with textured tape to ensure good traction and prevent slip. Eight angled idler wheels are used to share the load of the carriage and maintain it aligned with the rails at all times, acting as a passive linear bearing. The absolute linear speed of the carriage is measured externally by locating visual markers using the ARUCO library (Garrido-Jurado et al., 2014). This allows controlling the traversal speed of the wheel-leg and regulating its angular speed to simulate any desired slip condition and detect any slip event on the carriage-driving wheel.

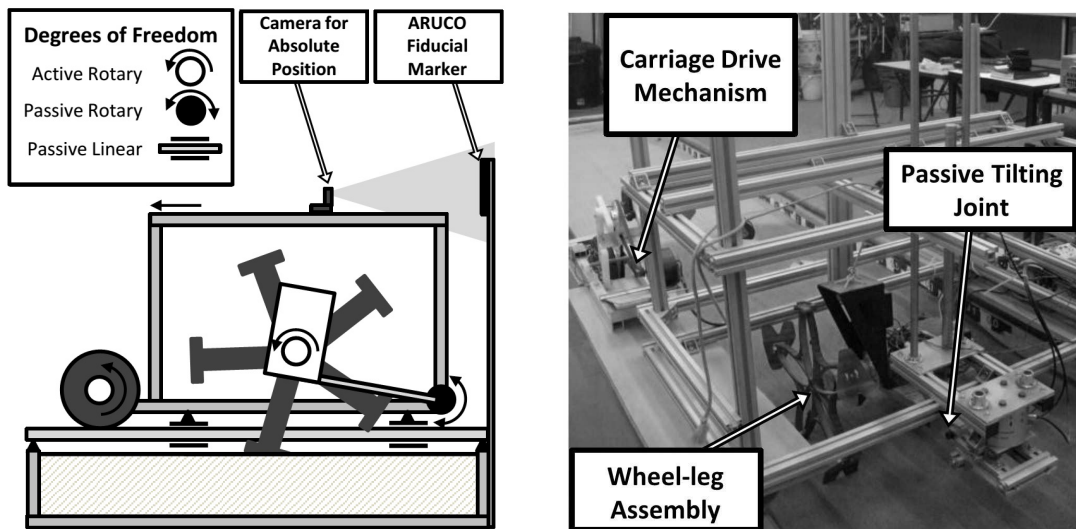


Figure 12: Degrees of freedom diagram (left) and labelled image (right) of the Single Wheel-Leg Test Bed

Before each test is performed using the SWLTB set-up in the laboratory, the soil was prepared using a consistent raking method to re-homogenize the structure of the soil disturbed by the previous test and minimise the variability of soil properties between tests due to different compaction states. The strength consistency of the prepared soil was evaluated before every test by performing Dynamic Cone Penetrometer tests (Lewinger et al., 2013) every 0.5 meters along the testbed. The total depth and depth per impact values were compared with values obtained during small-scale calibration tests on samples with known bulk densities. Whenever the differences were beyond the variability observed during those calibration tests, the soil was re-prepared before carrying out the SWLTB experiment. In addition, a vibration device was dragged along the soil surface for some experiments with SSC-3 soil, to achieve higher compaction levels and test the influence of bulk density of the same soil on wheel-leg sinkage. All tests performed with this set-up presented in this paper were carried out with all five spokes of the wheel-leg equipped with LTFs.

3.3 Field Testing Set-Up

Testing in more realistic conditions is important for an appropriate evaluation of the performance of the sensor system and to identify sources of errors that do not occur in the controlled laboratory environment. Field tests provide natural lighting conditions and terrain profiles, with heterogeneous soil compositions, slopes and irregular surfaces. The SWLTB set-up is designed to be easily adapted for attachment with any mobile platform. Using the in-house wheeled micro-rover SMART (Gao, Samperio, Shala, & Ye, 2012) experiments were carried out in the West Wittering beach in the southern English coast. The experiments consisted of forward driving runs over different types of terrain found on-site, including firm bedrock (path #1), compact flat SSC-3 sand (path #2) and loose duned SSC-3 sand (path #3) as shown in Fig. 13.

The passive rotary DoF of the SWLTB was linked with the chassis of the SMART rover, which replaces the moving carriage as seen in Fig. 14. Two different wheel-leg set-ups were used, combining LTFs in two non-consecutive legs with three carbon fibre feet or rubber feet as shown in Fig. 14 (left and right for carbon fibre feet and rubber feet respectively). This is done to prevent the intentionally high sinkage experienced by the LTF from excessively hindering the motion of the wheel-leg and to study the potential influence of the previous leg on the sinkage of the current leg. The wheel-leg speed command and data logging interfaces were set with the OBC of the SMART rover, which uses the same software framework as the SWLTB.

During all experiments, both under laboratory and field conditions, the mass of the wheel-leg assembly remained constant at 3.75 kg, in order to simulate the load of the 15 kg FASTER SR assuming even load distribution. Three independent repetitions were carried out on re-prepared soil (laboratory) for each test

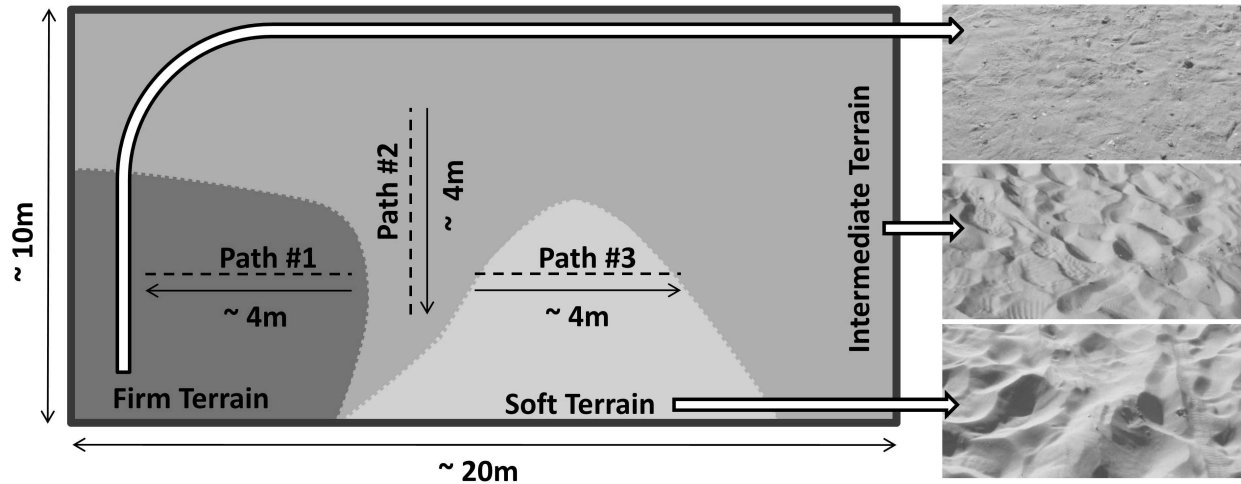


Figure 13: Diagram of the distribution of different types of terrain in the field testing site and the paths of the tests carried out (left) and images of the different types of terrain (right)

configuration, with an extra repetition for a total of four in tests on unprepared terrain (field). Each of these runs covered a distance of 4 m, yielding a minimum of approximately 60 independent leg stance cycles for each testing condition. These leg stance cycles are the samples used to calculate the statistical characteristics of the sensed data and the statistical performance of sinkage estimation and trafficability prediction.

The rotational speed of the wheel-leg was regulated to match the traversal speed of the SWLTB moving carriage and the SMART rover, so as to minimize wheel-leg slippage during the tests, with a desired traversal speed of 10 cm/s, and to focus on the independent analysis of wheel-leg sinkage. Actual slip levels were maintained below $\pm 5\%$ in normal testing conditions. Very rarely (less than 2% of all gathered leg cycles), the moving carriage or SMART rover underwent observable sudden slippage that caused actual wheel-leg

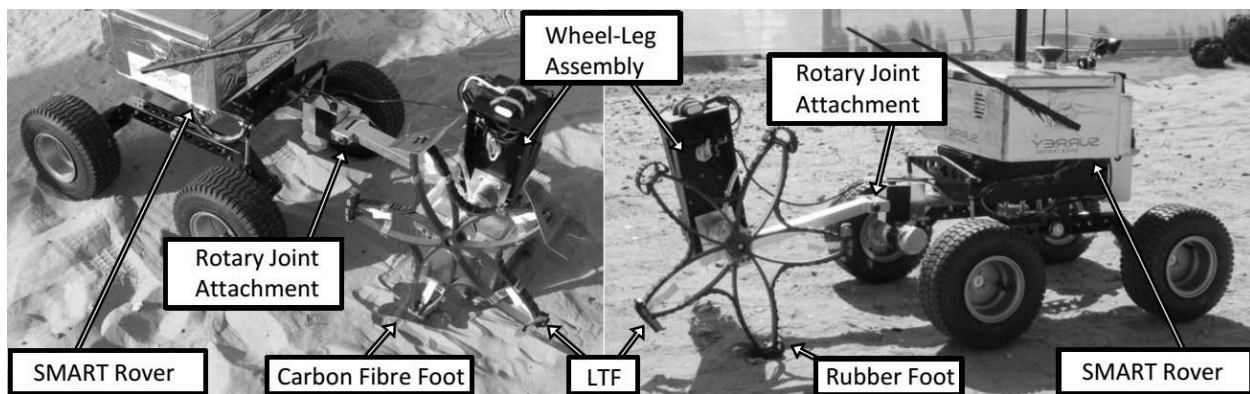


Figure 14: SWLTB attachment mounted on the SMART rover (Gao et al., 2012) for field testing, with both wheel-leg configurations used: LTF with carbon fibre feet (left) and with rubber feet (right - image horizontally mirrored for labelling purposes)

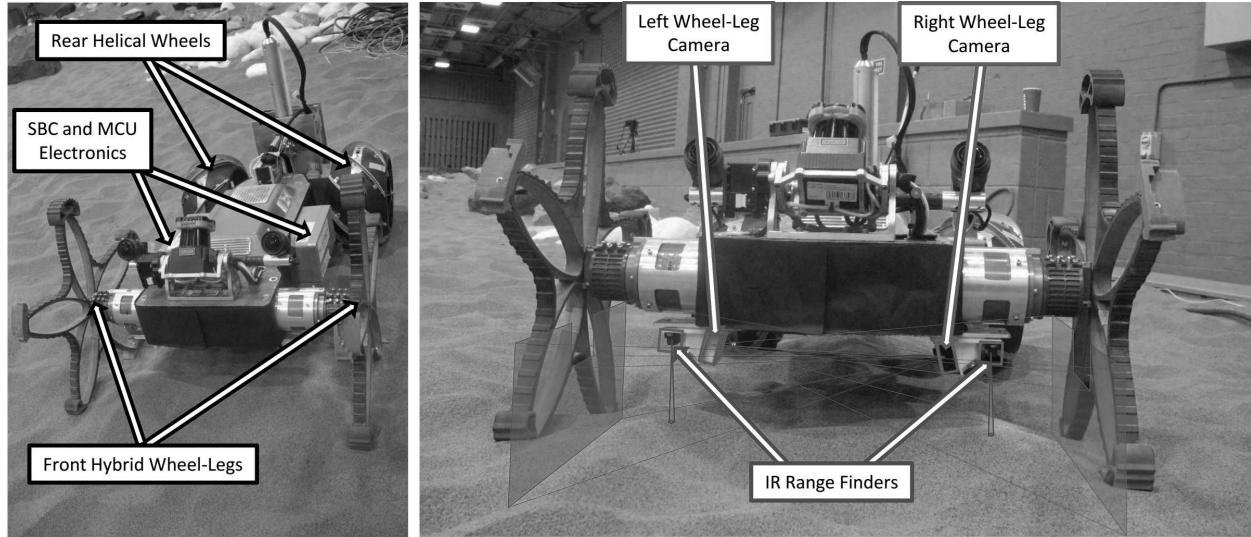


Figure 15: Wheel-leg sinkage detection hardware integrated on full FASTER SR (left), courtesy of FASTER (FASTER, 2013) with detailed front view of camera and IR ranger placement and their FoVs (right)

slip to raise beyond those thresholds. In these isolated cases, the leg cycles were excluded from the analysis due to potential slip-sinkage effects (Lyasko, 2010) that are beyond the scope of this paper.

3.4 Integration of Sinkage Detection Sensor System

For final validation under more representative operating conditions, tests were also carried out on a fully mobile robot. Two identical wheel-leg sinkage sensing systems, i.e. one for each of the two front wheel-legs, are integrated on-board the FASTER SR, whose design details can be found in (Sonsalla et al., 2013). The same hardware components and software framework used for the SWLTB are used, with a couple of differences. The SBCs are connected via-Ethernet to the SR's OBC, which also takes care of motor control and sensing the angular position of the wheel-legs and the attitude of the robot's body, hence replacing the dashed connections in Fig. 9. The sensor data from the substituted hardware components are retrieved in real time for on-line wheel-leg sinkage detection and trafficability prediction, queried via-software from the ROCK framework (Joyeux, Schwendner, Roehr, & Center, 2014) controlling the SR on the OBC. For this purpose, interfacing ROS nodes and a ROCK task are implemented and connected using a ROCK-ROS bridge that converts ROCK ports into ROS message topics. A laptop is still used to wirelessly access the OBC and SBCs, control the tests and log data.

The SBC, MCU and related electronics are placed in ad-hoc enclosures mounted on the sides of the SR chassis, as shown in Fig. 15 (left). The cameras and IR range finders are mounted on mirrored positions

of the chassis' underside, as in Fig. 15 (right), keeping the same distances to the wheel-leg's centre point as in the SWLTB set-up. This configuration leads to crossed camera FoVs, as the camera is placed on the opposite side to the sensed wheel-leg. Although this causes a slight image occlusion by the opposite camera module, a leg length above 100 mm is visible at all times, fitting the requirements of the system. The same feet configuration used for the laboratory SWLTB was used in all SR tests analysed in this paper.

4 Performance of Sinkage Detection Approaches

The performance of the sinkage detection was evaluated looking at different aspects: robustness of vision-based detection to environmental factors, precision of vision-based detection against manual image assessment, consistency of vision-based and clearance-based detection, sensitivity to foot and soil type and computational efficiency of the algorithm. All results presented in this section correspond to tests carried out with the SWLTB in the laboratory and in the field.

4.1 Robustness of vision-based algorithm

The robustness of the proposed vision algorithm to changing environments was tested, simulating in the laboratory even more challenging conditions than those found in the field. Rocks of various sizes and colours were placed in the background while running tests. Most of them were successfully filtered already in the edge detection step. Even granular gravel of similar contrast and size as the black and white pattern on the wheel-leg, which produced significant background noise after the edge detection step, was greatly reduced during the edge merging phase and led to correct detection of both sides of the leg as seen in Fig. 16 (left). Moreover, experiments were carried out in the laboratory both in complete darkness and with a single focused source of skewed incandescent back-light. In both cases the algorithm managed to correctly detect the leg.

Figure 16 (right) illustrates a particularly challenging image with gravel in the background, very bright sand lit by the LEDs due to the poor environmental lighting and the highly contrasting projected shadow of the leg. Even in these adverse conditions, the algorithm manages to filter all the noise and detect both sides of the leg. There is certain performance degradation, as the lower central section of the pattern is not properly merged and incorrectly filtered out, as marked by the grey ellipses. Nevertheless, errors due to such faults are limited to a few millimetres, as in this example.

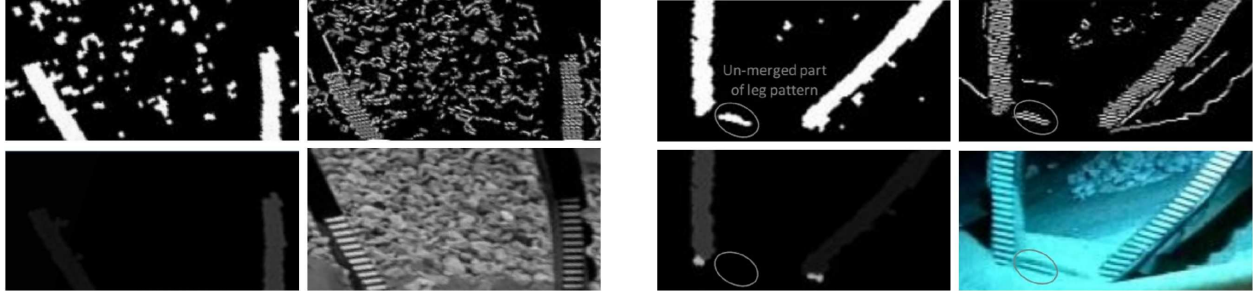


Figure 16: Details of raw, pre-processed and processed images using the edge-based sinkage detection algorithm on gravel (left) and with poor lighting (right)

One of the main lessons learned during the field trials is the significant effect of irregular terrain profiles over the sinkage estimated through computer vision methods. This implies that, when significant sinkage occurs, the leading and trailing sides of the leg are split in the image. Using the approach proposed in (Al-Milli et al., 2013) only the largest blob is chosen, therefore neglecting one of the sides of the leg. This is not problematic as long as the terrain remains parallel to the horizontal direction of the camera image frame, but it produces inaccuracies when the image frame tilts and/or the terrain is sloped, as in Fig. 17 (left).

Considering only the front or rear side of the leg results in a significant error as compared to the level of occlusion of the leg's centreline. However, this is tackled in the new VBDS approach by detecting both sides and averaging their sinkage estimates. To evaluate the performance of this functionality improvement with the edge-based algorithm, experiments were carried out using the SWLTB with artificial SSC-3 slopes of ± 7 degrees, each of them extending over three intervals: uphill, flat, and downhill.

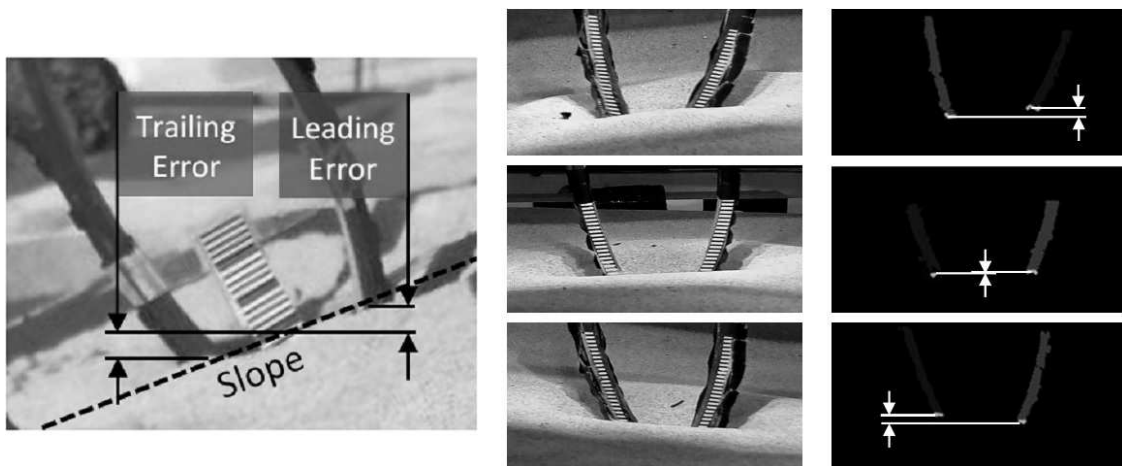


Figure 17: Examples of error induced by terrain slope on the detected sinkage for each of the sides of the leg on soft terrain (left) and difference between the sinkage of both leg sides (right) for uphill (top), flat (middle) and downhill (bottom) terrain

Table 3: Precision errors of the edge-based sinkage detection algorithm against manual image ground-truth on SSC-3 soil type

Soil Compaction	Dense	Loose	Dense	Loose
Background Conditions	Normal	Normal	With Rocks	Poor Lighting
Sinkage Avg. [mm]	30.5	46.6	33.2	52.0
Error Avg. [mm]	0.26	0.33	0.28	0.59
Error Std. Dev. [mm]	1.44	1.72	1.69	1.58
Relative Error Avg. [%]	1.60	1.06	1.14	2.56

Sample raw and processed images are displayed in Fig. 17 (right) for each of these conditions, with the detected sinkage difference between both leg sides indicated by the white lines and arrows. The difference between both sides qualitatively indicates the ability of the new approach to account for the trailing and leading slope errors observed. The quantitative improvement in performance will be assessed below in the analysis of sinkage detection accuracy.

4.2 Precision against manually assessed images

The precision of the sinkage estimates obtained by the vision-based algorithm can be evaluated by manually assessing the level of occlusion of the leg in each image captured by the camera. In order to take into account the slope effects mentioned above when setting the manual ground truth, the lowest un-occluded pixels of both edges of a leg were selected. The ground truth value was then obtained by inputting said values as $y_{px,L}$ and $y_{px,R}$ in Eq. (5).

Table 3 summarizes the precision errors computed for the different conditions tested on SSC-3 using the SWLTB in the laboratory. Tests on both loose and dense SSC-3 have average errors below a third of a millimetre and relative errors below 2%. The average error is slightly higher on loose soil due to the bigger soil depression around the legs, but the relative error is lower than for dense soil because of the higher sinkage. Tests carried out with rocks and gravel do not show a noticeable overall decrease in precision, with intermediate absolute and relative errors to those obtained on loose and dense SSC-3, quantitatively confirming the robustness of the algorithm to such conditions.

A significantly higher average for absolute and relative errors is experienced during tests in dark conditions, rising to nearly 0.6 mm and 2.6%, due to detection faults such as the one presented above in Fig. 16 (right). While these deviations can be mitigated using lower intensity LEDs or with a finer tuning of the edge detection and merging parameters the average error is still fairly low, in the same order of magnitude

as the pixel-to-mm ratio. The standard deviations on all testing conditions, including poor lighting, remain around 1.5 mm, showing the high precision of the algorithm.

These low error average values and variabilities are not necessarily indicative of the accuracy of the algorithm. Both the algorithm output and manual ground truth originate from the same input: the camera images. In consequence, the precision error does not account for potential systematic errors such as sinkage overestimation due to obstacles blocking the FoV of the camera or sinkage underestimation due to soil depression around the leg. However, since the laboratory soil preparations are flat and without FoV occluding obstacles these error values can be taken as good accuracy indicators in smooth terrain conditions.

4.3 Consistency of vision-based and clearance-based approaches

The clearance-based sinkage estimation using the IR was originally added to the sensor system to correct the potential systematic errors of vision-based sinkage detection mentioned above. Therefore, it can provide a good ground truth to evaluate the accuracy of the vision-based algorithm and quantify the improvement in using the VBDS approach over the original VBSS approach. Given the different frequency of the clearance-based and vision-based methods (50 Hz and 5 Hz respectively) all clearance-based estimates between consecutive vision-based estimates were averaged to calculate the error between both outputs.

The chart in Fig. 18 (left) shows the best Gaussian distribution fits of the obtained errors for the tests carried out with the SWLTB in the laboratory on SSC-3 in three different preparations: flat loose, flat dense and sloped. In all three cases the maximum probability of the error distribution using VBDS, represented with continuous lines, is higher than those using VBSS, marked with dashed lines, meaning that the results become more consistent. This consistency is significantly higher in the tests performed on dense SSC-3 than in those performed on loose SSC-3, probably due to a combined effect of the lower preparation homogeneity and the higher sinkages experienced in loose SSC-3.

The difference between VBDS and VBSS is much smaller for the sloped SSC-3 tests. Nevertheless, looking separately at the data corresponding to uphill and downhill sections as shown in Fig. 18 (right) reveals not only a similarly significant improvement in error consistency when using VBDS but also an even bigger reduction of the error bias. In spite of this improvement, the average error for both downhill and uphill tests is in the order of several millimetres, negative for the former and positive for the latter. However, these errors can be mostly accounted for with the slope-induced error modelled in Eq. (4). The average values for slope-induced errors calculated using the VBDS detected sinkage, the IMU estimated attitude and the

Table 4: Mean and standard deviation of vision-ranging sinkage differences and slope-induced error of ranging-based sinkage estimate on SSC-3

Soil Configuration	Flat Dense	Flat Loose	Sloped	Uphill	Downhill
VBSS-IR Difference Mean [mm]	0.13	1.31	0.66	3.89	-3.63
VBDS-IR Difference Mean [mm]	0.03	0.73	0.35	2.74	-1.71
VBSS-IR Difference Std. Dev. [mm]	2.28	4.07	6.71	2.81	8.44
VBDS-IR Difference Std. Dev. [mm]	1.77	3.41	6.51	2.32	7.73
IR Slope-Induced Mean Error [mm]	-	-	0.56	2.46	-1.74

manually measured terrain slope, are marked by the vertical dotted lines in Fig. 18 (right) and lie within a millimetre of the uphill and downhill error distribution mean values.

Table 4 summarizes the mean and standard deviations of the difference between vision-based and ranging-based sinkage estimates, as well as IR slope-induced errors, for the different testing conditions. The overall decrements of both the means and the standard deviations capture the improvement of using VBDS over VBSS. The close proximity between the IR slope-induced errors and the VBDS-IR difference mean confirms the good accuracy of the VBDS approach and the consistency of the vision-based and clearance-based methods even in sloped terrain.

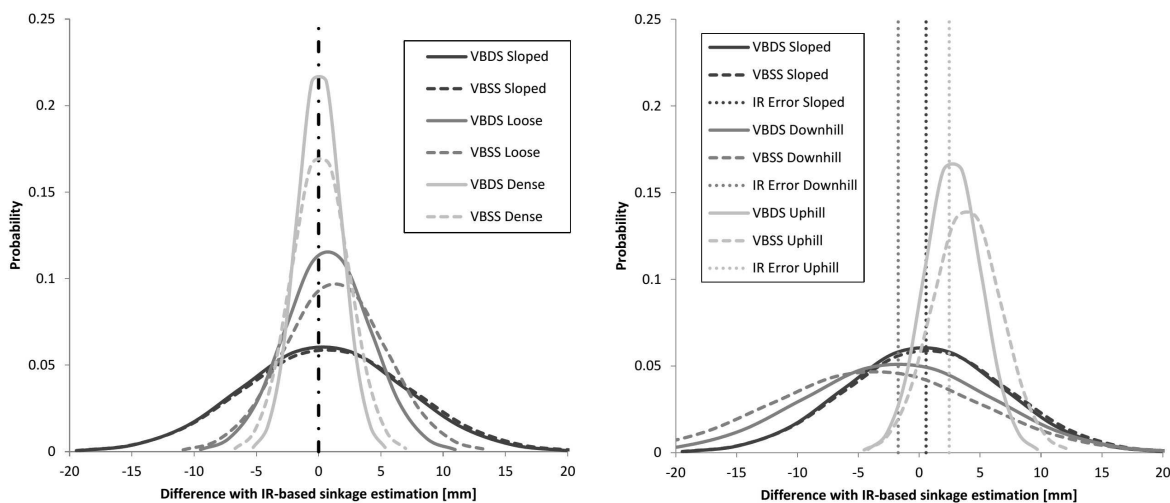


Figure 18: Fitted Gaussian distributions of the difference between clearance-based and vision-based sinkage estimates using single and dual contours with dense, loose, and sloped SSC-3 (left), and with uphill and downhill SSC-3 (right)

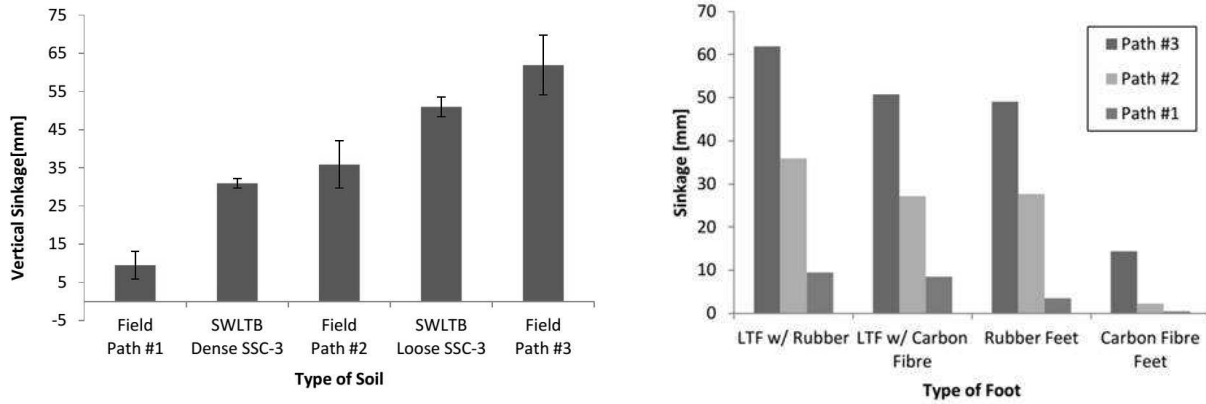


Figure 19: Average midstance sinkage detected for the LTF on different types of soil with one standard deviation error bars (left) and average midstance sinkage along the three paths tested on the field for the different type of feet configurations (left)

4.4 Influence of foot and soil types during field testing

Experiments performed during the field trials were not only useful for the qualitative observations previously discussed, e.g. slope-induced errors or robustness to environmental lighting. In addition, the differences between sensed sinkage in uneven, unprepared, natural terrain and flat, prepared, laboratory samples can be quantitatively analysed. In Fig. 19 (left) the average midstance sinkage detected with a single standard deviation for laboratory SSC-3 tests and the three types of field terrain are compared. The intermediate and soft terrains of paths #2 and #3 are expected to have similar sinkage values as dense and loose SSC-3, since this type of soil was directly sourced from the field testing site. However, mean sinkage values in the field are significantly higher than SWLTB values. This could be partially attributed to the lower compaction of sand when naturally deposited by aeolian processes rather than raked. On the other hand, the notably wider variability of field results than that of laboratory results suggests that the higher average values might be also due to larger soil compaction heterogeneity and/or sinkage overestimation. Even though the latter case would imply faulty trafficability assessments due to FoV occlusion by the frequent dunes, these are in the order of 1 cm and are conservative from a mobility safety standpoint. Meanwhile, the former case would result from correctly detected softer terrain, and is favoured by the fact that a similar variability is also observed in the low-sinkage firm ground of path #1.

Finally, the effect of mixed feet configurations on sensed sinkage is plotted in Fig. 19 (right). As expected, the rubber foot and carbon fibre foot experience significantly lower sinkage due to their lower and better distributed contact pressure, especially in the case of the carbon fibre foot. However, an important observation arises from the fact that LTF sinkage when the previous leg had a rubber foot is significantly higher

Table 5: Computational performance of vision-based sinkage detection algorithm using edge detection

	VBSS w/ Laptop	VBDS w/ Laptop	VBSS w/ SBC	VBDS w/ SBC
Frame rate [fps]	125.59	115.15	1.39	1.31
Segmentation [msec]	6.63 (83%)	6.65 (76%)	435.3 (61%)	436.5 (57%)
Detection [msec]	0.81 (10%)	1.55 (18%)	274.9 (38%)	316.9 (42%)

than when the previous leg had a carbon fibre foot. This indicates that, should a mixed foot configuration be used, the sinkage of the previous foot needs to be taken into account when assessing trafficability based on wheel-leg sinkage.

4.5 Vision-based detection computational efficiency

The computational performance of the vision-based sinkage estimation approaches using edge detection was measured. The algorithm was run both on a laptop, with a 2.8 GHz quad-core processor and 6 GB of RAM, and on the SBC used for the embedded implementation of the wheel-leg sinkage sensor system, with a 700 MHz processor and 512 MB of RAM. The processing times of the different stages of the algorithm were recorded on both platforms to compute the average frame processing rate achievable. With the higher processing resources of the laptop, frame rates are over 110 fps and up to 130 fps, thus the speed of the algorithm in real-time is only limited by the capture frame rate of the camera. With the lower computational resources of the embedded SBC, frame rates drop drastically to barely 1.3-1.4 fps, as shown in Table 5. In spite of the drop, these frame rates would still enable processing 3-4 images per leg stance cycle at the considered traversal speed of 10 cm/s, which is enough for the trafficability assessment method proposed in this paper.

The VBDS approach involves a higher processing overhead than the VBSS approach. However, given that the image capture and most of the image processing remains the same, the decrease in frame rate is marginal, with values only 5 – 10% lower than those achieved with VBSS. As expected, processing times during the segmentation phase are nearly identical for the VBDS and VBSS approaches, since the additional processing takes place only in the contour selection and sinkage estimation stages. The detection phase takes nearly twice as much time for the VBDS when running in the laptop, taking only 18% of the total processing time per frame. However, the detection phase has much closer values for both VBSS and VBDS when running on the SBC, taking 38-42% of the total time per frame. This suggests the existence of a bottleneck in the detection phase when running on the SBC that might give room to a partial frame rate improvement through code optimization.

Although the SBC used has the same amount of RAM as Curiosity’s computer system, the CPU clock speed is significantly higher (700 MHz vs. 132 MHz). Taking into consideration the effect of differences in their architecture (800 MIPS vs. 266-500 MIPS) and level of code optimization the gap can be narrowed down. Nevertheless, this highlights the tightness of the computational requirements of the vision-based approach with the resources of current planetary rovers. The clearance-based method, which has been proven to yield low relative errors with respect to the vision-based approach, does not present such a limitation, and would provide a simpler and more efficient solution to the problem.

5 Trafficability Prediction Modelling and Validation

Once the accuracy and robustness of the wheel-leg sinkage sensing methods proposed has been demonstrated, the next step is to establish a quantitative model that relates this magnitude to the trafficability characteristics of the terrain, determined through the terramechanics model described earlier.

5.1 Model of the Relationship Between Soil Trafficability and Wheel-Leg Sinkage

Simulations were carried out for each the four soil types using the terramechanics model previously presented in Section 2.5. The resulting values were then compared off-line to the detected wheel-leg sinkage obtained using the SWLTB set-up and experimental methodology described above. The comparison of the simulated wheel sinkage with the experimental midstance wheel-leg sinkage reveals a non-injective relationship, as seen in Fig. 20 (left) for a wheel of the PR. The lowest wheel-leg sinkage was experienced on SSC-2, while the simulated wheel sinkage was actually lower for ES-3, as could be expected from its higher normal load bearing stiffness. In addition, the sinkage of the wheel is higher than that of the wheel-leg (markers are above the dashed line) with the only exception of ES-3.

These observations indicate that sensed wheel-leg sinkage is neither a conclusive nor a conservative indicator of wheel sinkage on the same soil. However, the purpose of this research is not to predict wheel sinkage, but soil trafficability. When comparing sensed wheel-leg sinkage and tractive efficiency, as shown in the plots of Fig. 20 (middle and right), the relationship becomes both injective and approximately linear. These graphs also show that this linearity is maintained when varying the wheel parameters used in the simulation. Increasing the radius of the wheel for a constant mass leads to a higher tractive efficiency, while increasing the mass reduces the efficiency.

Based on these empirical observations, a linear model is proposed to obtain the tractive efficiency of the soil from wheel-leg midstance sinakge, as shown in Eq. (11). The model's efficiency-intercept (c_a) and sinkage-gradient (c_b) are specific to a given wheel, defined by the M-R parameter pair, and are calculated through least-squares linear regression. These parameters are derived solely based on the SWLTB experimental data for soils SSC-2 and SSC-3, in order to evaluate the robustness of the model for interpolated (ES-3) and extrapolated (ES-1) data points.

$$\zeta_{z,WL} = \zeta_z(\theta_W = 0) \quad \rightarrow \quad \eta_{d,e}(\zeta_{z,WL}) = c_a + c_b \zeta_{z,WL} \quad (11)$$

The parameters and coefficient of determination (R^2) of the least-square linear fits plotted as dashed lines in Fig. 20 (middle and right) are summarized in Table 6. The high R^2 values support the strong linear correlation between both magnitudes, in spite of the lower values observed when approaching the lower and higher extremes of the considered mass and radius ranges respectively. This suggests significant non-linearities occurring towards these extremes, which can be studied through a detailed parametric analysis.

5.2 Parametric Generalization of the Model

With the aim of developing a generalized model for parametrized wheels, simulations were performed for a range of wheel radii and masses in the 5 – 25 cm and 10 – 90 kg ranges respectively. The intercept parameter

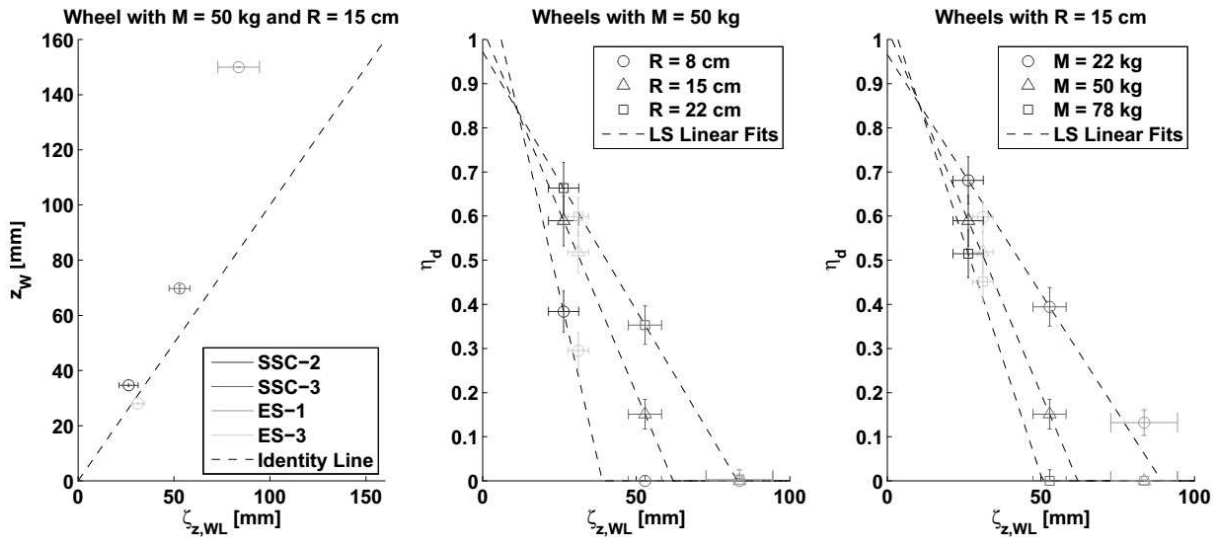


Figure 20: Correlation of wheel-leg detected sinkage with terramechanics-based PR wheel sinkage (left) and with tractive efficiency of wheels with varying masses (middle) and varying radii (right)

Table 6: Parameters and R^2 coefficients of least square linear fits of experimental wheel-leg sinkage vs. simulated wheel trafficability data

Wheel Mass [kg]	Wheel Radius [cm]	Intercept c_a	Slope c_b [mm^{-1}]	R^2 Coefficient
50	8	1.184	-0.030	0.77
50	15	1.025	-0.017	0.95
50	22	0.972	-0.012	0.97
22	15	0.966	-0.011	0.97
78	15	1.074	-0.021	0.70

(c_a) represents the traction efficiency when the wheel-leg experiences no sinkage. Its empirical values tend to one, implying perfectly efficient traction, which is consistent with the lack of rolling or soil compaction resistance forces on rigid ground. However, a continuous ridge rises for low radii across all simulated masses, going up to ≈ 1.2 before dropping towards 0.5 for even lower radii, as shown in Fig. 21 (far-left). An opposite trend is observed on the gradient (c_b), as it presents a valley in the same low-radius region, as seen in Fig. 21 (mid-left). The effect of these anomalous parameter variations on the wheel-leg midstance sinkage to wheel tractive efficiency relationship is plotted in Fig. 21 for the minimum wheel radius (mid-right) and maximum wheel mass (far-right) simulated. Empirical values of the gradient parameter are negative, as expected from the increasing resistive forces for higher sinkages. Its sensitivity to different wheel radii is inversely proportional, while it maintains a direct linear relationship with wheel mass. As a result of this analysis, the generalized model in Eq. (12) is proposed.

$$\eta_{d,g} = 1 + k_\eta \zeta_{z,WL} = 1 + \frac{k_{\eta,1} + k_{\eta,2}M}{R} \zeta_{z,WL} \quad , \quad R \in (0.055 + 0.0014M, 0.075 + 0.0049M) \quad (12)$$

The efficiency-intercept is fixed to 1, representing perfect tractive efficiency for zero wheel-leg sinkage, and the sinkage-gradient linearly varies with M and is inversely proportional to R , physically representing the inverse of the minimum wheel-leg sinkage for zero tractive efficiency. The only two parameters of this model ($k_{\eta,1-2}$) are specific to the wheel-leg used during the experiments. These generalizations yield errors below 5% relative to the empirical model parameters (c_{a-b}) for wheel radii within the interval specified on the right hand side of Eq. (12) and bounded by the two straight black lines in Fig. 21 (left). This modified model combines the strengths of computational simplicity, thanks to its linear nature, and of generality over different types of soils and wheel operating conditions.

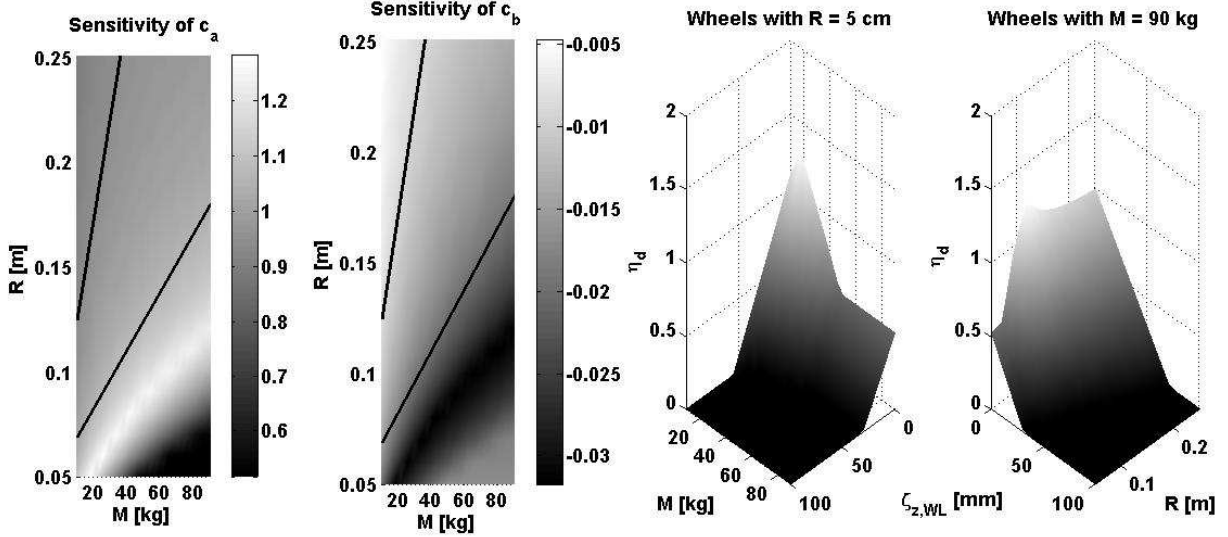


Figure 21: Sensitivity of the empirical linear fit coefficients to wheel parameters (far-left and mid-left) and sensitivity of wheel tractive efficiency as a function of wheel-leg sinkage for $R = 5$ cm (mid-right) and for $M = 90$ kg (far-right)

5.3 Validation on Full Wheel-Legged Rover

In order to validate the empirical and generalized models for tractive efficiency prediction using sensed wheel-leg sinkage and compare their accuracy, an independent test campaign was carried out using the full FASTER SR and the same soil preparation methodology used for the SWLTB experiments.

The Root-Mean-Square Error (RMSE) between the terramechanics-based simulation and wheel-leg sinkage prediction of tractive efficiency was calculated for all SR tests and wheel M-R pairs. Soil-specific and global results using the empirical model are plotted in Fig. 22. Values are well below 15%, with the only exception of SSC-2 soil in the low-radii region. Within the boundaries of accurate generalization specified in Eq. (12), marked by the straight black lines, values are generally below 10%, down to values around 5% for the global error across all soil types. The two softer soils, i.e. SSC-3 and ES-1, have a distinct behaviour in that their low-radii and high-masses region is dominated by very low and even zero (below the white line) errors. This is due to very low or null efficiency values, correctly predicted by the empirical wheel-leg sinkage model.

This circumstance also occurs when applying the generalized model, as seen by the null Mean Errors (ME) in those same regions for SSC-3 and ES-1, plotted in Fig. 23. The low-radii and high-mass region shows a tendency of the model to underestimate tractive efficiency, as seen from the dark colours in the graphs, leading to conservative trafficability predictions. On the other hand, the low-mass and high-radii region yields over-predictions, as seen from the lighter colours.

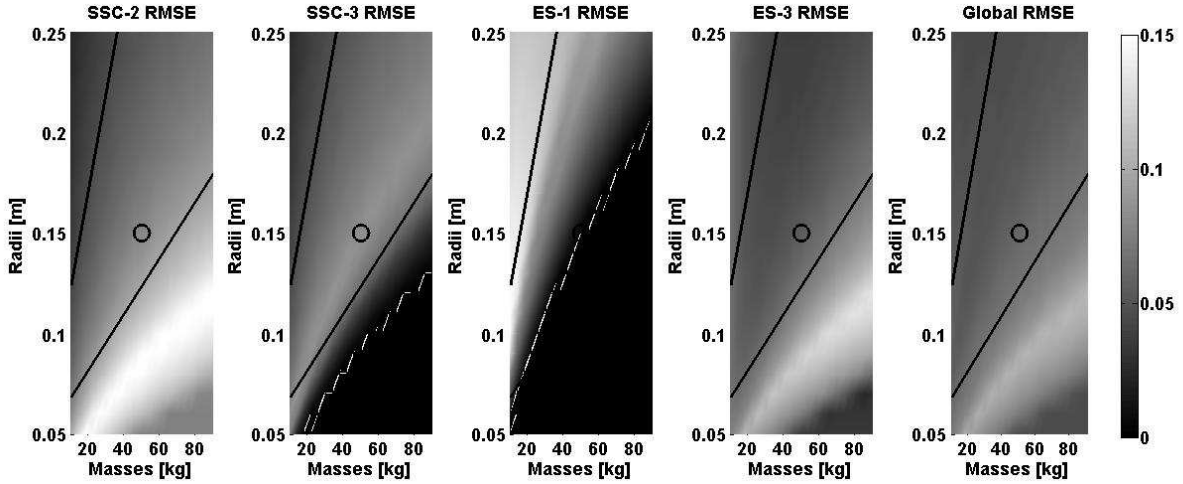


Figure 22: Sensitivity to wheel parameters of the RMS Error of tractive efficiency calculated with the empirical model for different types of soil

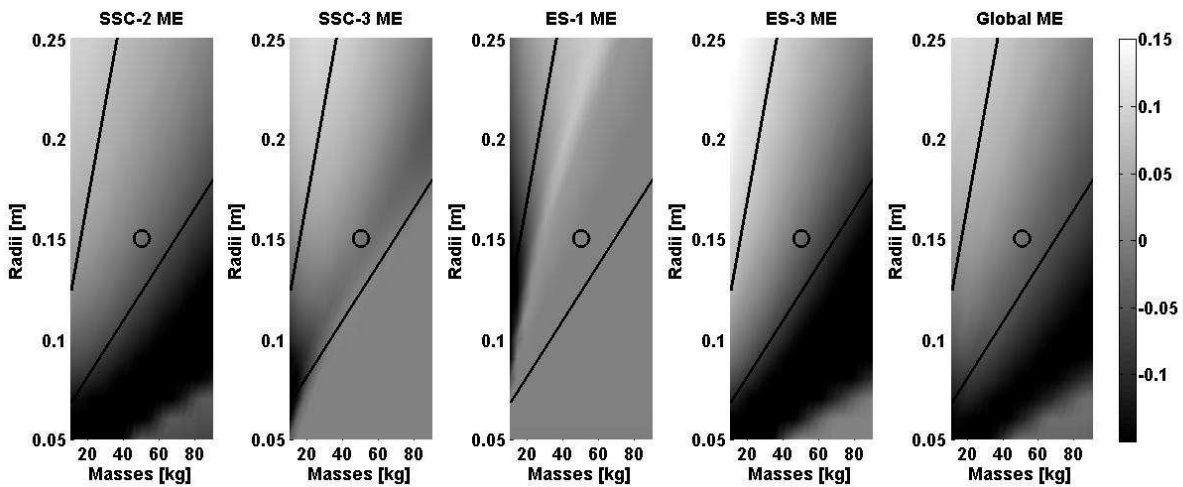


Figure 23: Sensitivity to wheel parameters of the Mean Error of tractive efficiency calculated with the generalized model for different types of soil

Once again, the absolute values within the marked linear boundaries are almost ubiquitously below the 10% threshold. The point corresponding to the configuration of the FASTER PR wheels, in the centre of the black circles in both Fig. 22 and 23, lies close to the line of zero error separating the over-estimation region from the underestimation region, slightly biased towards the latter. This makes it a good solution for safe trafficability estimation in this specific case-scenario.

Table 7: Averages and standard deviations of RMS Errors of predicted tractive efficiency in full SR experiments vs. terramechanics-based simulation results for the complete and restricted M-R ranges

Tested Soils	SSC-2	SSC-3	ES-1	ES-3	Global
Empirical [%]	8.26 (± 3.37)	4.55 (± 3.06)	4.15 (± 4.91)	6.40 (± 2.51)	6.29 (± 1.73)
Empirical (Restr.) [%]	6.74 (± 1.24)	7.02 (± 1.05)	5.26 (± 3.97)	4.98 (± 0.86)	5.46 (± 0.60)
General [%]	11.66 (± 6.13)	5.34 (± 4.14)	4.14 (± 5.25)	10.75 (± 6.57)	10.62 (± 4.76)
General (Restr.) [%]	7.79 (± 1.72)	8.20 (± 2.14)	5.77 (± 4.91)	6.66 (± 1.97)	7.59 (± 1.50)

5.4 Comparison of the Empirical and Generalized Models for Trafficability Assessment

In order to compare the accuracy of the empirical and generalized models, the mean and standard deviations of the RMSE across all simulated M-R pairs and only within the restricted linear boundaries were calculated, as summarized in Table 7. Nearly all values are below 10%, even going below 5% in some cases. Considering only the restricted M-R region consistently reduces the standard deviation of the RMSE values by 1-4%. However, it has opposite effects on the mean RMSE values. For stiff soils, i.e. SSC-2 and ES-3, the mean value decreases around 1.5% for the empirical model and as much as 4% for the generalized model. For the softer soils, i.e. ES-1 and SSC-3, the mean value actually increases by 1-3%. This is partly expected from the very low RMSE values observed above in the low-radius and high-mass region, and it brings the mean values closer to those of the stiffer soils and to the global mean across all soil types.

The generalized model does experience a slight accuracy degradation relative to the empirical model, but maintains acceptable overall values, with a 7.59% average RMSE error across all SR test data. It is remarkable that the error values for the two soil types that were not used to fit the empirical model parameters, i.e. ES-1 and ES-3, have even lower average RMSE values (both with the empirical and generalized models) than the two soil types that were actually used for that purpose, i.e. SSC-2 and SSC-3. This demonstrates the robustness of these models to different and unknown types of soil.

When looking at the specific configuration of the FASTER PR wheel in Table 8, the terramechanics-based simulations estimate a good tractive efficiency of $\approx 60\%$ for SSC-2, slightly better than that of ES-3 at $\approx 50\%$. Much poorer performance is expected on SSC-3, as the efficiency drops down to $\approx 15\%$, while it is actually null for ES-1. The wheel-leg sinkage empirical model proposed predicts extremely close values, with a global underestimation ME below 1%. The generalized model also underestimates the tractive efficiency on average, with a slightly bigger global ME but still below 3%. Standard deviations of the predictions for each of the soil types using the generalized model are even lower than those of the empirical model itself.

Table 8: Mean wheel tractive efficiency for FASTER PR wheel on each soil type and global Mean Errors

Tested Soils	$\bar{\eta}_{d,SSC-2}$	$\bar{\eta}_{d,SSC-3}$	$\bar{\eta}_{d,ES-1}$	$\bar{\eta}_{d,ES-3}$	Global ME
Terramechanics [%]	58.94 (± 5.70)	15.12 (± 3.37)	0.00 (± 0.00)	51.85 (± 4.62)	-
Empirical [%]	58.94 (± 8.18)	15.15 (± 8.86)	0.03 (± 0.08)	51.05 (± 5.58)	-0.13 (± 0.91)
General [%]	57.04 (± 8.07)	13.95 (± 8.58)	0.00 (± 0.00)	49.26 (± 5.51)	-2.69 (± 7.63)

6 Conclusions and Future Work

Two alternative methods for wheel-leg sinkage detection have been proposed. The first one improves existing wheel and wheel-leg vision-based techniques. It increases robustness to lightning and background conditions through edge detection and merging, and ad-hoc LED illumination. It also reduces errors induced by irregular and sloped terrain by detecting both sides of the hollow legs (VBDS) rather than only one (VBSS). Its computational efficiency is comparable to other vision-based approaches, and permits real-time execution although the results suggest that the computational requirements might be too high for current planetary applications, unless the rover briefly stops the wheel-leg at leg midstance.

The second method models ground-clearance to estimate wheel-leg sinkage based on range finder measurements. The low estimate errors and its immunity to dust covering the wheel-leg prove this new approach as a reliable and computationally efficient complement/substitute to the vision-based solution. The model is sensitive to errors on significantly sloped terrains, although this can be corrected through the proposed model if a local slope estimate is available.

Lessons learned from field testing include the fact that hybrid foot configurations should be considered carefully, as they significantly influence the sinkage of a given type of foot on the same terrain. Naturally shaped terrains with marked dunes are likely to produce higher sinkage variability due to more heterogeneous soil compaction states or to sinkage overestimation due to FoV occlusion. Either way, sinkage detection is sufficiently accurate or conservative, thus fitting the purpose of safely detecting non-geometric hazards. Moreover, such wavy terrains could be considered as geometric rather than non-geometric hazards and detected remotely.

An empirical linear model has been proposed to predict terrain trafficability based on terramechanics tractive efficiency through wheel-leg sinkage detection. The model is also generalized for a wide range of wheel parametric configurations in terms of mass and radius. The model parameters were derived empirically from tests on only a sub-set of two soils using a simplified single wheel-leg test bed. The models were then

independently validated using the fully mobile SR on a wider set of four significantly different dry frictional soils, with a range of predicted tractive efficiency in the 0 – 60% interval for the PR wheel.

Both the empirical and generalized model show good accuracy and can reliably predict the tractive efficiency based on wheel-leg sinkage, with a slight underestimation in the specific case of the PR wheel that favours mission safety. However, they render the initial criterion of static load sinkage correlation for foot design insufficient, as the relations between dynamic wheel sinkage and wheel-leg sinkage or tractive efficiency are not injective. Wheel rolling sinkage is more heavily dominated by the load bearing stiffness of the soil, while wheel-leg rolling sinkage and tractive efficiency show a similarly higher sensitivity to the shear strength properties of the soil.

Although their usefulness has been proven, the developed wheel-leg sinkage-based trafficability models themselves cannot produce separate estimates of the load bearing and shear strength parameters of the soil. Therefore, future work will deal with sensing wheel-leg slippage and analysing stick-slip and slip-sinkage events to obtain a more thorough soil characterisation while still exploiting the advantages of on-line wheel-leg-soil interaction sensing. Finally, an analytical model for parametric, multi-legged, light-weight wheel-legs interacting with deformable soil is under investigation for further generalization and to fill the gap between existing models for rimmed wheels and for ultra-light, single-legged wheel-legs.

Some other interesting guidelines for future work unaddressed by the scope of this paper include: exploring the behaviour of the wheel-leg on highly cohesive soils, quantifying in more detail the effect of soil relative density on the proposed models, experimentally re-validating the terramechanics model used for wheel tractive efficiency simulation, evaluating the feasibility of using structured light as a substitute for the vision-based and/or clearance-based sinkage estimation methods proposed, improving the prediction variability of the models by accounting for the uncertainty introduced by neglected factors, e.g. leg compliance, and studying the implications of the Triple Leg Stance phase, regarding the possible influence of the inter-leg structure.

Acknowledgements

The FASTER project is funded by the EU Seventh Framework Program, under grant agreement no. 284419. The work presented in this paper is also funded by a European Postgraduate Scholarship of Fundacion Obra Social “laCaixa”. The authors wish to acknowledge the FASTER Consortium, in particular Roland Sonsalla

(DFKI) for designing, building and providing the wheel-leg model and the fully mobile rover used for testing, and the Surrey Space Centre STAR-Lab field trials team, especially Conrad Spiteri, Dr. Said Al-Milli and Prof. Yang Gao for providing the SMART rover for testing and the colour-based sinkage detection algorithm code used for benchmarking purposes in this paper.

References

- Allouis, E., Marc, R., Gancet, J., Nevatia, Y., Cantori, F., Sonsalla, R., . . . Richter, L. (2015, May). FP7 FASTER project - demonstration of multi-platform operation for safer planetary traverses. In *Proceedings of the 13th Symposium on Advanced Space Technologies in Robotics and Automation (ASTRA '15)*. Noordwijk (Netherlands).
- Al-Milli, S., Spiteri, C., Comin, F., & Gao, Y. (2013, November). Real-time vision based dynamic sinkage detection for exploration rovers. In *IEEE/RSJ International Conference on Intelligent Robots and Systems (IROS '13)* (pp. 4675–4680). Tokyo (Japan).
- Arvidson, R. E., Anderson, R., Bartlett, P., Bell, J., Blaney, D., Christensen, P., . . . Wilson, J. (2004). Localization and physical properties experiments conducted by Spirit at Gusev crater. *Science*, *305*(5685), 821–824.
- Bekker, M. G. (1960). *Off-road locomotion: Research and development in Terramechanics*. Ann Arbor: The University of Michigan Press.
- Benet, G., Blanes, F., Simó, J. E., & Pérez, P. (2002). Using infrared sensors for distance measurement in mobile robots. *Robotics and autonomous systems*, *40*(4), 255–266.
- Broderick, J. A., Tilbury, D. M., & Atkins, E. M. (2014). Characterizing energy usage of a commercially available ground robot: Method and results. *Journal of Field Robotics*, *31*(3), 441–454.
- Brooks, C., & Iagnemma, K. (2005). Vibration-based terrain classification for planetary exploration rovers. *IEEE Transactions on Robotics*, *21*(6), 1185–1191.
- Brooks, C. A., Iagnemma, K. D., & Dubowsky, S. (2006). Visual wheel sinkage measurement for planetary rover mobility characterization. *Autonomous Robots*, *21*(1), 55–64.
- Canny, J. (1986). A computational approach to edge detection. *IEEE Transactions on Pattern Analysis and Machine Intelligence*, *8*(6), 679–698.
- Coleman, M. J. (2010). Dynamics and stability of a rimless spoked wheel: A simple 2D system with impacts. *Dynamical Systems*, *25*(2), 215–238.
- David, L. (2005). *Opportunity Mars Rover stuck in sand*. <http://www.space.com/1019-opportunity-mars->

- rover-stuck-sand.html. ([Online; accessed 27-November-2015])
- Ding, L., Deng, Z., Gao, H., Tao, J., Iagnemma, K. D., & Liu, G. (2015). Interaction mechanics model for rigid driving wheels of planetary rovers moving on sandy terrain with consideration of multiple physical effects. *Journal of Field Robotics*, *32*(6), 827–859.
- FASTER. (2013). <http://www.faster-fp7-space.eu>. ([Online; accessed 27-November-2015])
- Fu, Q., & Krovi, V. (2008, October). Articulated wheeled robots: Exploiting reconfigurability and redundancy. In *ASME 2008 Dynamic Systems and Control Conference* (pp. 653–660). Ann Arbor (USA).
- Gallina, A., Krenn, R., Scharringhausen, M., Uhl, T., & Schäfer, B. (2014). Parameter identification of a planetary rover wheel–soil contact model via a bayesian approach. *Journal of Field Robotics*, *31*(1), 161–175.
- Gao, Y., Samperio, R., Shala, K., & Ye, C. (2012). Modular design for planetary rover autonomous navigation software using ROS. *Acta Futura*, *5*(2012), 9–16.
- Garrido-Jurado, S., Muñoz-Salinas, R., Madrid-Cuevas, F. J., & Marín-Jiménez, M. J. (2014). Automatic generation and detection of highly reliable fiducial markers under occlusion. *Pattern Recognition*, *47*(6), 2280–2292.
- Gouache, T. P., Patel, N., Brunskill, C., Scott, G. P., Saaj, C. M., Matthews, M., & Cui, L. (2011). Soil simulant sourcing for the ExoMars rover testbed. *Planetary and Space Science*, *59*(8), 779–787.
- Grotzinger, J. P., Crisp, J., Vasavada, A. R., Anderson, R. C., Baker, C. J., Barry, R., . . . Wiens, R. C. (2012). Mars Science Laboratory mission and science investigation. *Space Science Reviews*, *170*(1-4), 5–56.
- Helmick, D., Angelova, A., & Matthies, L. (2009). Terrain adaptive navigation for planetary rovers. *Journal of Field Robotics*, *26*(4), 391–410.
- Hidalgo, J. (2013, May). Navigation and slip kinematics for high performance motion models. In *Proceedings of the 12th Symposium on Advanced Space Technologies in Robotics and Automation (ASTRA '13)*. Noordwijk (Netherlands).
- Howard, A., & Seraji, H. (2001). Vision-based terrain characterization and traversability assessment. *Journal of Robotic Systems*, *18*(10), 577–587.
- Iagnemma, K., Kang, S., Shibly, H., & Dubowsky, S. (2004). Online terrain parameter estimation for wheeled mobile robots with application to planetary rovers. *IEEE Transactions on Robotics*, *20*(5), 921–927.
- Iagnemma, K., & Ward, C. C. (2009). Classification-based wheel slip detection and detector fusion for mobile robots on outdoor terrain. *Autonomous Robots*, *26*(1), 33–46.
- Irani, R., Bauer, R., & Warkentin, A. (2011). A dynamic terramechanic model for small lightweight vehicles with rigid wheels and grousers operating in sandy soil. *Journal of Terramechanics*, *48*(4), 307–318.

- Janosi, Z., & Hamamoto, B. (1961, June). Analytical determination of drawbar pull as a function of slip for tracked vehicles in deformable soils. In *1st International Conference of the International Society for Terrain-Vehicle Systems (ISTVS '61)*. Turin (Italy).
- Joyeux, S., Schwendner, J., Roehr, T. M., & Center, R. I. (2014, May). Modular software for an autonomous space rover. In *Proceedings of the 12th International Symposium on Artificial Intelligence, Robotics and Automation in Space (i-SAIRAS '14)*. Montreal (Canada).
- Kim, J., & Lee, J. (2013). Predicting maximum traction to improve maneuverability for autonomous mobile robots on rough terrain. *Journal of Automation and Control Engineering*, *1*(1), 1–6.
- Krebs, A., Pradalier, C., & Siegwart, R. (2010). Adaptive rover behavior based on online empirical evaluation: Rover–terrain interaction and near-to-far learning. *Journal of Field Robotics*, *27*(2), 158–180.
- Lewinger, W. A., Comin, F., Ransom, S., Richter, L., Al-Milli, S., Spiteri, C., . . . Saaaj, C. (2013, May). Multi-level soil sensing systems to identify safe trafficability areas for extra-planetary rovers. In *Proceedings of the 12th Symposium on Advanced Space Technologies in Robotics and Automation (ASTRA '13)*. Noordwijk (Netherlands).
- Li, C., Zhang, T., & Goldman, D. I. (2013). A terradynamics of legged locomotion on granular media. *Science*, *339*(6126), 1408–1412.
- Li, T., Chang, S. J., & Tong, W. (2004). Fuzzy target tracking control of autonomous mobile robots by using infrared sensors. *IEEE Transactions on Fuzzy Systems*, *12*(4), 491–501.
- Lyasko, M. (2010). Slip sinkage effect in soil–vehicle mechanics. *Journal of Terramechanics*, *47*(1), 21–31.
- Mahony, R., Cha, S. H., & Hamel, T. (2006, December). A coupled estimation and control analysis for attitude stabilisation of mini aerial vehicles. In *Proceedings of the Australasian Conference on Robotics and Automation* (Vol. 225). Auckland (New Zealand).
- Maimone, M., Cheng, Y., & Matthies, L. (2007). Two years of visual odometry on the Mars Exploration Rovers. *Journal of Field Robotics*, *24*(3), 169–186.
- Manduchi, R., Castano, A., Talukder, A., & Matthies, L. (2005). Obstacle detection and terrain classification for autonomous off-road navigation. *Autonomous robots*, *18*(1), 81–102.
- Matson, J. (2010). Unfree Spirit: NASA’s Mars Rover appears stuck for good. *Scientific American*, *302*(4), 16.
- Milella, A., Reina, G., & Siegwart, R. (2006). Computer vision methods for improved mobile robot state estimation in challenging terrains. *Journal of Multimedia*, *1*(7), 49–61.
- Mutch, T. A., Arvidson, R. E., Binder, A. B., Guinness, E. A., & Morris, E. C. (1977). The geology of the viking lander 2 site. *Journal of Geophysical Research*, *82*(28), 4452–4467.
- NASA. (2010). <http://mars.nasa.gov/mer/gallery/all/spirit.html>. ([Online; accessed 27-November-2015])

- Nevatia, Y., Bulens, F., Gancet, J., Gao, Y., Al-Mili, S., Sonsalla, R., ... Richter, L. (2013, May). Safe long-range travel for planetary rovers through forward sensing. In *Proceedings of the 12th Symposium on Advanced Space Technologies in Robotics and Automation (ASTRA '13)*. Noordwijk (Netherlands).
- Ojeda, L., Borenstein, J., Witus, G., & Karlsen, R. (2006). Terrain characterization and classification with a mobile robot. *Journal of Field Robotics*, *23*(2), 103–122.
- Ojeda, L., Cruz, D., Reina, G., & Borenstein, J. (2006). Current-based slippage detection and odometry correction for mobile robots and planetary rovers. *IEEE Transactions on Robotics*, *22*(2), 366–378.
- Perumpral, J. V., Liljedahl, J. B., & Perloff, W. H. (1971). A numerical method for predicting the stress distribution and soil deformation under a tractor wheel. *Journal of Terramechanics*, *1*(8), 9–22.
- Peynot, T., Lui, S.-T., McAllister, R., Fitch, R., & Sukkarieh, S. (2014). Learned stochastic mobility prediction for planning with control uncertainty on unstructured terrain. *Journal of Field Robotics*, *31*(6), 969–995.
- Pommerol, A., Schmitt, B., Beck, P., & Brissaud, O. (2009). Water sorption on martian regolith analogs: Thermodynamics and near-infrared reflectance spectroscopy. *Icarus*, *204*(1), 114–136.
- Quinn, R. D., Offi, J. T., Kingsley, D. A., & Ritzmann, R. E. (2002, October). Improved mobility through abstracted biological principles. In *IEEE/RSJ International Conference on Intelligent Robots and Systems (IROS '02)* (Vol. 3, pp. 2652–2657). Lausanne (Switzerland).
- Reina, G., Ishigami, G., Nagatani, K., & Yoshida, K. (2008, May). Vision-based estimation of slip angle for mobile robots and planetary rovers. In *IEEE International Conference on Robotics and Automation (ICRA '08)* (pp. 486–491). Pasadena (USA).
- Saranli, U., Buehler, M., & Koditschek, D. E. (2001). RHex: A simple and highly mobile hexapod robot. *The International Journal of Robotics Research*, *20*(7), 616–631.
- Schroer, R. T., Boggess, M. J., Bachmann, R. J., Quinn, R. D., & Ritzmann, R. E. (2004, April). Comparing cockroach and Whegs robot body motions. In *IEEE International Conference on Robotics and Automation (ICRA '04)* (Vol. 4, pp. 3288–3293). New Orleans (USA).
- Schwendner, J., Grimminger, F., Bartsch, S., Kaupisch, T., Yuksel, M., Bresser, A., ... Kirchner, F. (2009, October). CESAR: A lunar crater exploration and sample return robot. In *IEEE/RSJ International Conference on Intelligent Robots and Systems (IROS '09)* (pp. 3355–3360). St. Louis (USA).
- Scott, G. P., & Saa, C. M. (2012). The development of a soil trafficability model for legged vehicles on granular soils. *Journal of Terramechanics*, *49*(3), 133–146.
- Skonieczny, K., Moreland, S. J., Asnani, V. M., Creager, C. M., Inotsume, H., & Wettergreen, D. S. (2014). Visualizing and analyzing machine-soil interactions using computer vision. *Journal of Field Robotics*, *31*(5), 820–836.

- Sonsalla, R. U., Ahmed, M., Fritsche, M., Akpo, J. B., Vögele, T., & RIC, D. (2014, September). Scout rover applications for forward acquisition of soil and terrain data. In *European Planetary Science Congress* (Vol. 9, p. 819). Cascais (Portugal).
- Sonsalla, R. U., Fritsche, M., Vögele, T., & Kirchner, F. (2013, May). Concept study for the FASTER micro scout rover. In *Proceedings 12th Symposium on Advanced Space Technologies in Robotics and Automation (ASTRA '13)*. Noordwijk (Netherlands).
- Sonsalla, R. U., Nevatia, Y., Fritsche, M., Akpo, J. B., Gancet, J., Kirchner, F., & RIC, D. (2014, June). Design of a high mobile micro rover within a dual rover configuration for autonomous operations. In *Proceedings of the 12th Int. Symp. on Artificial Intelligence, Robotics and Automation in Space (i-Sairas '14)*. Montreal (Canada).
- Wall, M. (2014). *Curiosity Rover on Mars stalled by 'Hidden Valley' sand trap*. <http://www.space.com/26866-mars-rover-curiosity-driving-sand-trap.html>. ([Online; accessed 27-November-2015])
- Weiss, C., Fechner, N., Stark, M., & Zell, A. (2007, September). Comparison of different approaches to vibration-based terrain classification. In *Proceedings of the 3rd European Conference on Mobile Robots* (pp. 7–12). Freiburg (Germany).
- Wong, J. (1980). Data processing methodology in the characterization of the mechanical properties of terrain. *Journal of Terramechanics*, 17(1), 13–41.
- Wong, J.-Y., & Reece, A. (1967). Prediction of rigid wheel performance based on the analysis of soil-wheel stresses part I. performance of driven rigid wheels. *Journal of Terramechanics*, 4(1), 81–98.
- Zacny, K., Wilson, J., Craft, J., Asnani, V., Oravec, H., Creager, C., ... Fong, T. (2010, March). Robotic lunar geotechnical tool. In *12th International Conference on Engineering, Science, Construction, and Operations in Challenging Environments (ASCE Earth and Space '10)*. Honolulu (USA).